

# 1 An integrated single-cell reference atlas of the human endometrium.

2 Magda Marečková<sup>1,2±</sup>, Luz Garcia-Alonso<sup>1±</sup>, Marie Moullet<sup>1</sup>, Valentina Lorenzi<sup>1</sup>, Robert Petryszak<sup>1</sup>,  
3 Carmen Sancho-Serra<sup>1</sup>, Agnes Oszlanczi<sup>1</sup>, Cecilia Icoresi Mazzeo<sup>1</sup>, Sophie Hoffman<sup>1</sup>, Michał  
4 Krassowski<sup>2,3</sup>, Kurtis Garbutt<sup>2</sup>, Iva Kelava<sup>1</sup>, Kezia Gaitskell<sup>4,5</sup>, Slaveya Yancheva<sup>5</sup>, Ee Von Woon<sup>6,7</sup>,  
5 Victoria Male<sup>6</sup>, Ingrid Granne<sup>2</sup>, Karin Hellner<sup>2</sup>, Krishnaa T Mahbubani<sup>8,9</sup>, Kourosh Saeb-Parsy<sup>9,10</sup>,  
6 Mohammad Lotfollahi<sup>1</sup>, Elena Prigmore<sup>1</sup>, Jennifer Southcombe<sup>2</sup>, Rebecca A Dragovic<sup>2</sup>, Christian M  
7 Becker<sup>2</sup>, Krina T Zondervan<sup>2,3@</sup>, Roser Vento-Tormo<sup>1@</sup>

8

9 1 Wellcome Sanger Institute, Cambridge, UK

10 2 Oxford Endometriosis Care Centre, Nuffield Department of Women's & Reproductive Health,  
11 University of Oxford, Oxford, UK

12 3 Wellcome Centre for Human Genetics, University of Oxford, Oxford, UK

13 4 Nuffield Division of Clinical Laboratory Sciences, Radcliffe Department of Medicine, University of  
14 Oxford, Oxford, UK

15 5 Department of Cellular Pathology, John Radcliffe Hospital, Oxford, UK

16 6 Department of Metabolism, Digestion and Reproduction, Institute of Developmental Reproductive  
17 and Developmental Biology, Imperial College London, London, UK

18 7 The Fertility Centre, Chelsea and Westminster Hospital, London, UK

19 8 Department of Haematology, University of Cambridge, Cambridge, UK

20 9 Cambridge Biorepository for Translational Medicine (CBTM), NIHR Cambridge Biomedical  
21 Research Centre, Cambridge, UK

22 10 Department of Surgery, University of Cambridge, Cambridge, UK

23

24 ±co-first

25 [@ rv4@sanger.ac.uk](mailto:rv4@sanger.ac.uk) (Roser Vento-Tormo) and [krina.zondervan@wrh.ox.ac.uk](mailto:krina.zondervan@wrh.ox.ac.uk) (Krina T Zondervan)

## 26 **Abstract**

27 The human endometrium, the inner lining of the uterus, exhibits complex, dynamic changes  
28 throughout the menstrual cycle in response to ovarian hormones. Aberrant response of  
29 endometrial cells to hormones is associated with multiple disorders, including endometriosis.  
30 Previous single-cell studies of the endometrium profiled a limited number of donors and lacked  
31 consensus in defining cell types and states. Here, we introduce the Human Endometrial Cell  
32 Atlas (HECA), a high-resolution single-cell reference atlas, combining published and newly  
33 generated single-cell transcriptomics datasets of endometrial biopsies of women with and  
34 without endometriosis. The HECA assigned consensus cell types and states, and uncovered  
35 novel ones, which we mapped *in situ* using spatial transcriptomics. We quantified how  
36 coordinated interactions between cell states in space and time contribute to endometrial  
37 regeneration and differentiation. In the continuously changing *functionalis* layer, we identified  
38 an intricate coordination of TGFβ signalling between stromal and epithelial cells, likely crucial  
39 for cell differentiation. In the *basalis* layer, we defined signalling between fibroblasts and a new  
40 epithelial cell population expressing epithelial stem/progenitor markers, suggesting their role  
41 in endometrial regeneration. Additionally, integrating the HECA single-cell data with genome-  
42 wide association study data and comparing endometrial samples from women with and without  
43 endometriosis, we pinpointed subsets of decidualised stromal cells and macrophages as the  
44 most dysregulated cell states in endometriosis. Overall, the HECA is an invaluable resource  
45 for studying endometrial physiology, investigating endometrial disorders, and guiding the  
46 creation of endometrial microphysiological *in vitro* systems.

## 47 Main

48 Human reproduction depends on the endometrium, the inner mucosal lining of the uterus. It  
49 prepares an optimal environment for embryo implantation and supports pregnancy if  
50 implantation is successful. In the absence of a pregnancy, the endometrium sheds each month  
51 during menstruation. Morphologically, the endometrium is composed of two layers: the ever-  
52 changing *functionalis* (adjacent to the uterine cavity) and the relatively constant *basalis*  
53 (adjacent to the myometrium). In response to ovarian steroid hormones, the *functionalis*  
54 undergoes repeated cycles of shedding and repair without scarring, extensive growth and  
55 differentiation<sup>1,2</sup>.

56

57 At the cellular level, the endometrium has a heterogeneous architecture. The endometrial  
58 epithelium consists of a horizontally interconnected network of *basalis* glands<sup>3-5</sup> contiguous  
59 with coiled *functionalis* glands extending vertically towards the uterine cavity, where a layer of  
60 *functionalis* luminal cells lines the endometrial surface. The *basalis* glands harbour epithelial  
61 stem/progenitor cells needed to regenerate the *functionalis* layer after menstruation<sup>6-10</sup>. The  
62 *functionalis* epithelium provides a site for embryo implantation, and produces secretions to  
63 nourish it. Stromal, fibroblast, perivascular and endothelial cells provide support and structural  
64 integrity, including rich vasculature within the tissue. An array of immune cells play crucial  
65 roles in endometrial shedding and repair<sup>11,12</sup>, as well as embryo implantation<sup>13</sup>. Cell-cell  
66 communication between the endometrial cells is key in maintaining tissue homeostasis and  
67 menstrual cycle progression.

68

69 During female reproductive years, the endometrium is highly heterogeneous, both inter- and  
70 intra-individually, and thus a large sample size is required to account for the dynamic changes  
71 it undergoes both in time (across the menstrual cycle) and space (across different tissue  
72 microenvironments). In recent years, several foundational studies atlasing the cellular  
73 composition of the human endometrium in health and pathologies with single cell<sup>14-21</sup> and  
74 spatial<sup>15-17</sup> technologies have been published. However, these cell censuses have so far  
75 profiled a limited number of samples, lacked even coverage of the menstrual cycle phases,  
76 and lacked consensus cell state annotation and reproducible marker gene signatures. In  
77 addition, they varied considerably in terms of clinical and phenotypic characterisation of the  
78 individuals from whom the samples were obtained. These factors have complicated  
79 comparisons across studies, with, for example, inconsistencies in the identification and  
80 naming of epithelial and stromal cell states. An integrated single-cell reference atlas of the  
81 human endometrium, encompassing the widest possible range of cell states and samples, is  
82 now warranted.

83

84 Endometrial heterogeneity is further increased by endometrial/uterine disorders which are  
85 highly prevalent globally. For example, abnormal menstrual bleeding affects up to a third of all  
86 women in their lives, ~417,000 new cases of endometrial cancer are diagnosed yearly, and  
87 ~190 million women world-wide suffer from endometriosis<sup>22-24</sup>. In endometriosis, endometrial-  
88 like cells grow outside of the uterus (i.e. ectopically), and are associated with debilitating  
89 chronic pain and subfertility that can have a substantial negative impact on quality of life<sup>25</sup>.  
90 Conflicting evidence exists about whether and to what extent the endometrium itself (i.e. the  
91 eutopic endometrium) differs between those with and without endometriosis<sup>26,27</sup>. Recently,  
92 single-cell studies analysing small sample sizes, reported dysregulation of the stromal and  
93 immune compartments in the endometrium of women with endometriosis to various

94 degrees<sup>16,18,20,28,29</sup>. Larger sample sets are now needed if we are to unpick whether and how  
95 the endometrium differs in those with and without the condition. In this context, well-annotated  
96 reference cell atlases can provide invaluable insights.  
97

98 Here, we assemble a consensus cell atlas of the endometrium, the Human Endometrial Cell  
99 Atlas (HECA), by harmonising the transcriptomic and donor metadata information of ~626,000  
100 cells and nuclei from previously published and newly generated datasets  
101 (<https://www.reproductivecellatlas.org/>). We identify new cell populations, including an  
102 epithelial CDH2+ population in the *basalis* and distinct populations of *functionalis* epithelial  
103 and stromal cells characteristic of the early secretory phase. We describe the molecular  
104 signals likely mediating the spatiotemporal organisation and function of cellular niches  
105 throughout the menstrual cycle and provide a new interactive portal to visualise and query the  
106 predicted cell-cell communication. Finally, we use the HECA to give cellular context to genetic  
107 associations identified by the largest endometriosis genome-wide association study (GWAS)  
108 meta-analysis<sup>30</sup>. This analysis identifies macrophages and subsets of decidualised stromal  
109 cells as the endometrial cell types expressing the genes affected by the variants associated  
110 with endometriosis.  
111

## 112 **Results**

### 113 Harmonised data to generate the HECA

114 To comprehensively define endometrial cell types and states and how they change across the  
115 menstrual cycle, we analysed a total of ~626,000 high-quality cells and nuclei from 121  
116 individuals (**Figure 1a-b**). We started by creating a single-cell reference atlas, which we  
117 termed the HECA (**Figure 1c**). To create the HECA, we integrated six publicly available single-  
118 cell RNA sequencing (scRNA-seq) datasets (Wang et al.<sup>14</sup>, Garcia-Alonso et al.<sup>15</sup>, Tan et al.<sup>16</sup>,  
119 Lai et al.<sup>19</sup>, Fonseca et al.<sup>17</sup>, Huang et al.<sup>18</sup>) with our newly generated dataset (termed  
120 Mareckova (cells) dataset) (**Figure 1b**). Harmonisation of metadata across the studies and  
121 application of strict data quality control filters (**see Methods**) was essential for the integration.  
122 The final integrated HECA consisted of ~314,000 high-quality cells from 7 datasets, of which  
123 ~76,000 cells were newly profiled by us (**Supplementary Table 2**). It included a total of 63  
124 individuals both with endometriosis (i.e cases) and without endometriosis (i.e. controls), with  
125 samples collected either during natural cycles or when taking exogenous hormones (**Figure**  
126 **1b & c, Supplementary Table 1**). The majority of samples analysed were superficial biopsies  
127 of the endometrium, predominantly sampling the *functionalis* layer from living donors. Three  
128 samples from the uteri of donors who died of non-gynaecological causes contained full-  
129 thickness endometrium, encompassing both the *functionalis* and *basalis* layers, with attached  
130 subjacent myometrium.  
131

132 We observed striking differences between the cellular composition of the integrated scRNA-  
133 seq datasets, with variable recovery of epithelial, mesenchymal, endothelial and immune cells  
134 (Figure 1e). Choice of tissue digestion protocol, sampling bias (technical variation), menstrual  
135 cycle stage and use of exogenous hormones (biological variation) could all be responsible for  
136 the differences observed (**see Methods & Supplementary Figure 1 & Supplementary Table**  
137 **1**). The dataset-specific cellular proportions prompted us to generate an independent single-

138 nucleus RNA sequencing (snRNA-seq) dataset for 63 additional donors (**Figure 1b & d**). The  
139 large number of individuals in this dataset allowed us to overcome the technical variation  
140 introduced when data are generated by different laboratories. We profiled ~312,000 high-  
141 quality nuclei from snap-frozen samples of superficial endometrial biopsies (**Figure 1b & d**,  
142 **Supplementary Figure 2**, **Supplementary Table 2**), collected during natural cycles, when  
143 taking exogenous hormones, and included samples for donors with and without endometriosis  
144 (**Figure 1b**). Together, this dataset represents the largest set of human endometrial samples  
145 profiled at the single-cell-/nucleus transcriptomic level by a single laboratory so far. To align  
146 the cell state annotations across the scRNA-seq and snRNA-seq datasets, and determine the  
147 robustness of the HECA, we transferred cell states labels between datasets using machine  
148 learning tools (**see Methods**). Out of the endometrial cells identified by scRNA-seq, the  
149 majority were validated in the nuclei dataset (**Supplementary Figure 2b-c**).  
150

151 As expected, the majority of the cell populations were of endometrial origin, but the atlas also  
152 contained populations exclusively present in the myometrium from the whole uterine samples  
153 (e.g. uterine smooth muscle cells (uSMCs) and myometrial perivascular cells (mPV)). In  
154 addition, we detected a small number of mesenchymal HOXA13+ and epithelial KRT5+ cells,  
155 which based on their marker gene expression were likely cervical cell contamination. This was  
156 supported by their transcriptomic similarity to cervical cells when we compared the HECA with  
157 a publicly available scRNA-seq dataset of the cervix<sup>31</sup> (**Supplementary Figure 1e-i**). We did  
158 not detect any endometriosis-specific cell state in neither the scRNA-seq nor snRNA-seq data,  
159 providing further evidence that at the cellular level of the endometrium, differences between  
160 controls and cases may be more subtle. However, additional cell states appeared in samples  
161 from donors taking exogenous hormones, indicating that exogenous hormones strongly  
162 impact the global transcriptome of epithelial cells, an observation supported by both data  
163 sources (**Supplementary Figure 3**).  
164

165 Altogether, we generated the most comprehensive reference atlas of the human endometrium  
166 (i.e. the HECA), which can now be used to map and contextualise newly processed samples  
167 and external datasets using the transfer learning framework scArches<sup>32</sup>. To facilitate this  
168 process, we prepared computational tutorials (**see Methods**) and provide the weights from  
169 the trained scANVI model<sup>33</sup> of the HECA available at <https://www.reproductivecellatlas.org/>.  
170

## 171 Spatiotemporal complexity of the endometrial epithelium

172 The endometrial epithelium consists of a complex network of *basalis* glands, which house the  
173 stem/progenitor cells needed to regenerate the *functionalis* glands extending into the uterine  
174 cavity, lined by a layer of luminal cells (**Figure 1a**). Here, we characterised, with fine  
175 granularity, the cell states forming the different regions of the endometrial epithelium across  
176 the proliferative and secretory phases of the menstrual cycle.

177 We identified a novel population, the SOX9 basalis (CDH2+) cells, that was not reported by  
178 previous single-cell transcriptomics atlases. These cells expressed markers described for  
179 endometrial epithelial stem/progenitor cells (SOX9, CDH2, AXIN2, ALDH1A1<sup>9,34,35</sup>) (**Figure**  
180 **2a**). Using spatial transcriptomics and single molecule fluorescence *in situ* hybridisation  
181 (smFISH) imaging, we mapped this population to the *basalis* glands region in full thickness  
182 endometrial biopsies from both proliferative and secretory phases (**Figure 2b-c**). Cell-cell

183 interaction analyses indicated that the SOX9 basalis (*CDH2*+) population interacts with the  
184 fibroblast basalis (i.e. Fibroblast basalis *C7*+) population via the expression of CXCR4 and  
185 CXCL12, respectively (**Figure 2d**). The CXCL12/CXCR4 axis is known to have a role in the  
186 maintenance of the stem cell niche in other tissues<sup>36</sup>, providing further evidence for the  
187 stem/progenitor nature of this cell subset.

188

189 The cellular composition of the *functionalis* glands showed highly dynamic changes across  
190 the proliferative and secretory phases (**Figure 2a**). During the proliferative phase, we  
191 uncovered further heterogeneity within the known SOX9+ cell population<sup>15</sup>. Specifically, we  
192 identified two SOX9+ subpopulations: SOX9 *functionalis* I and II, which we mapped to the  
193 *functionalis* glands (**Supplementary Figure 4a**). The SOX9 *functionalis* I population  
194 expressed *CDH2*, high levels of SOX9 and was marked by the expression of *PHLDA1* and  
195 *SLC7A11*. The SOX9 *functionalis* II population exhibited lower expression of SOX9, was  
196 negative for *CDH2* and distinctly expressed *KMO*, *IHH* and *EMID1*. The luminal proliferative  
197 epithelium was defined by the presence of SOX9 luminal (*LGR5*+) pre-ciliated and ciliated  
198 cells (**Figure 1f, 2a**), as previously described by us<sup>15</sup>. As expected, we also detected a larger  
199 proportion of cycling epithelial cells in the proliferative phase endometrium (**Figure 1f**).

200

201 During the secretory phase, the SOX9+ populations were markedly reduced as the  
202 endometrium underwent further differentiation in order to prepare a receptive environment for  
203 blastocyst implantation (**Figure 1f**). During the differentiation process, both the glandular and  
204 luminal epithelium undergo dramatic transcriptomic and morphological changes. Having a  
205 larger number of samples allowed us to further subdivide the secretory phase into early, early-  
206 mid, mid and late secretory phases and define the populations associated with these stages  
207 (**Figure 1f, see Methods**). For the first time, we uncovered the transcriptomic profiles of cells  
208 characteristic of the *functionalis* layer during the early secretory phase (i.e. the preGlandular  
209 and preLuminal populations; **Figure 2a & e-f**). These populations were transcriptomically  
210 similar to the previously described glandular and luminal populations<sup>15</sup>, but appeared at earlier  
211 stages of the cycle and expressed markers not defined previously. For the preGlandular  
212 population these included *OPRK1*, *SUFU*, *CBR3*, *HPRT1*, and for the preLuminal population  
213 *SULT1E1* was the most specific marker (**Figure 2a**). Using spatial transcriptomics, we  
214 confidently mapped both populations to early, but not mid-secretory samples. Specifically, the  
215 preLuminal population mapped to the lumen and the preGlandular population to the  
216 *functionalis* glands (**Figure 2f & Supplementary Figure 4b**). We further confirmed the  
217 preGlandular subset using smFISH imaging (**Figure 2e & Supplementary Figure 4c**).

218

219 The number of preGlandular and preLuminal cells decreased in the early-mid and mid-  
220 secretory phase samples, with the dominant cell states being the previously described  
221 glandular, luminal and ciliated populations<sup>15</sup> (**Figure 1f**). Lastly, analysing a single sample  
222 profiled from the late secretory phase, we observed the presence of a glandular secretory  
223 population that upregulated *FGF7*, a mitogen found to have a role in wound healing in other  
224 contexts<sup>37,38</sup>.

225

226 We detected a previously described population of MUC5B epithelial cells<sup>16</sup> expressing  
227 *MUC5B*, *TFF3*, *SAA1*, *BPIFB1*. As in previous studies<sup>16</sup>, we also observed varied expression  
228 of the cell type marker *MUC5B* when staining full-thickness endometrial biopsies using  
229 smFISH (**Supplementary Figure 4d**). However, when projecting a publicly available scRNA-  
230 seq dataset of the cervix<sup>31</sup> onto our HECA (**Supplementary Figure 1h**), we found a cluster of

231 cervical epithelial cells matching the transcriptome of this population (**Supplementary Figure**  
232 **1g-i**). This result implies the *MUC5B*<sup>+</sup> cells are likely to be present in the endocervical  
233 columnar epithelial cells<sup>31,39</sup>, and we cannot disregard the possibility that in the HECA, the  
234 *MUC5B* population comes exclusively from the endocervix.  
235

236 In summary, we defined and spatially located novel epithelial cell states across the proliferative  
237 and secretory phases, including a putative stem/progenitor cell population found within the  
238 *basalis* layer and multiple transitory cell states dominating the *functionalis* layer.  
239

## 240 Stromal-epithelial crosstalk across the menstrual cycle

241 During the menstrual cycle, stromal and epithelial cells synchronise their differentiation under  
242 the influence of ovarian hormones, as well as locally produced paracrine factors. Here we  
243 used the HECA's fine-grained classification of stromal and epithelial cell states across the  
244 menstrual cycle to infer cell-cell communication occurring *in vivo* along the endometrial cellular  
245 niches in space (i.e. *basalis*, *functionalis*) and time (i.e. menstrual cycle phase).  
246

247 Within the *functionalis* layer, endometrial stromal cells (eStromal) specific to the proliferative  
248 phase and decidualised stromal cells (dStromal) specific to the secretory phase were defined  
249 previously at the single-cell level<sup>15,40</sup>. In the HECA, we further identified a new type of eStromal  
250 cells (eStromal MMPs) in samples collected during the menstrual and early proliferative  
251 phases (**Figure 3a**, **Supplementary Figure 1d**), characterised by the upregulation of  
252 metalloproteases (*MMP1*, *MMP10*, *MMP3*) and inhibin A (*INHBA*) (**Figure 3a**).  
253

254 In secretory phase samples, we identified three new dStromal cell states appearing at different  
255 stages of the secretory phase. Early decidualised stromal cells (dStromal early) were enriched  
256 in the early secretory phase samples and upregulated the progesterone-induced gene  
257 *PLCL1*<sup>41</sup> (**Figure 3a-b**). The mid decidualised stromal population (dStromal mid) mapped to  
258 early-mid and mid-secretory phase samples and upregulated *DKK1* (**Figure 3a-b**), a WNT-  
259 inhibitor crucial for the differentiation of epithelial secretory glands<sup>15</sup>. Late decidualised stromal  
260 cells (dStromal late) were present in both mid- and late secretory phase samples (**Figure 1f**)  
261 and upregulated the premenstrual marker *LEFTY2*<sup>42</sup> (**Figure 3a**). Both the dStromal mid and  
262 late populations downregulated oestrogen and progesterone receptors (*ESR1* and *PGR*).  
263

264 We uncovered an intricate spatiotemporal regulation of transforming growth factor beta  
265 (TGF $\beta$ ) signalling (**Figure 3c**). Specifically, the TGF $\beta$  superfamily receptors were ubiquitously  
266 expressed by all epithelial and stromal cells at all stages of the menstrual cycle  
267 (**Supplementary Figure 5**). Meanwhile, the ligands of TGF $\beta$  and growth differentiation factor  
268 (GDF) subfamilies (*TGFB1* and *GDF7*, respectively) were upregulated by all stromal cells until  
269 mid/late secretory phase, when expression dropped (**Figure 3c**). Interestingly, the activity of  
270 TGF $\beta$  signalling appeared confined within specific spatial and temporal boundaries by its  
271 antagonists, *LEFTY1* and *LEFTY2*. On one hand, *LEFTY1* was expressed by epithelial cells  
272 of the lumen (ciliated and luminal) and *LEFTY2* by uSMCs of the myometrium (**Figure 3c**).  
273 This pattern of expression likely establishes a top-bottom spatial boundary of TGF $\beta$  activity.  
274 On the other hand, the temporal boundary seemed to be determined by the expression of  
275 *LEFTY2* as well as *SMAD7* (the inhibitor of SMADs, downstream effectors of TGF $\beta$ ). These  
276 two molecules were expressed by the dStromal late population (**Figure 3a**), suggesting TGF $\beta$

277 activity is switched off towards the end of the menstrual cycle (**Figure 3d**). Additionally, using  
278 our detailed cell annotation, we could pinpoint the specific stromal cell states involved in  
279 previously reported stromal-to-epithelial cell signalling mediated by WNT inhibition<sup>40</sup>, insulin<sup>43</sup>  
280 and retinoic acid<sup>44</sup> across the menstrual cycle (**Figure 3c & d**).  
281

282 Taken together, our data supported a rise in TGFβ, insulin, WNT and retinoic acid signalling  
283 from early stages of the proliferative phase (**Figure 3d**). WNT inhibition marked the beginning  
284 of the secretory phase with the initiation of stromal cell decidualisation. In the late secretory  
285 phase, our data supported a signalling switch in the use of TGFβ signalling, insulin growth  
286 factors and retinoic acid metabolism (**Figure 3c & d**). The full collection of cell-cell  
287 communication factors, identified through CellPhoneDB analyses<sup>45</sup> can be visualised and  
288 queried using our new interactive portal at <https://www.reproductivecellatlas.org>.  
289

## 290 Macrophages in endometrial regeneration

291 To gain insights into the diversity and dynamics of innate immune cells in the endometrium  
292 and pinpoint their involvement in the regeneration process, we examined our comprehensive  
293 datasets ( $n = 32,322$  cells and  $n = 24,820$  nuclei). These datasets captured the three uterine  
294 Natural Killer cell populations (uNK1, uNK2, uNK3) and the two uterine macrophage  
295 populations (uM1 and uM2) previously identified by us in the endometrium during pregnancy  
296 (i.e. decidua)<sup>46</sup> (**Figure 4a, Supplementary Figure 6a-e**). Differential cell abundance analysis  
297 (**see Methods**) demonstrated an increase in the abundance of uNK1 cells during the secretory  
298 phase, in line with previous reports of granular endometrial immune cells proliferating during  
299 the secretory phase<sup>47,48</sup> (**Figure 4b, Supplementary Figure 6f**). Cell abundance of the other  
300 immune cell types did not differ between the proliferative and secretory phases.  
301

302 To deepen our understanding of the role innate immune cells play in endometrial regeneration,  
303 we interrogated their cell-cell communication with stromal, endothelial and perivascular (PV)  
304 cells. We focused on significantly upregulated genes in uMs and uNK cells when compared to  
305 all immune cell subsets, especially during the menstrual and proliferative phase, a period when  
306 these innate immune cells are thought to aid in endometrial wound healing and regrowth (**see**  
307 **Methods**). We found that the eStromal MMPs population (characteristic of the menstrual  
308 phase) expressed integrins and cytokines (CCL5, RARRES2) which can bind their cognate  
309 receptors upregulated by uMs (CCR1, CCRL2) (**Figure 4c; Supplementary Figure 7a**). This  
310 interaction likely supports the previously described recruitment of uMs to the tissue during  
311 menstruation<sup>49,50</sup>. We also noticed that uMs upregulated PDGFB, a protein from the PDGF  
312 family, known for their role in wound healing and repair in various tissues<sup>51,52</sup>. In the  
313 endometrium, it could operate by binding to the PDGFRB receptor, which is upregulated by  
314 eStromal MMPs (**Figure 4c**). Additionally, uMs upregulated TNF (uM1), as well as growth  
315 factors such as IGF1 (uM2) and EREG (uM1). These could stimulate the proliferation and  
316 survival of eStromal MMPs and proliferative eStromal cells by binding to their corresponding  
317 receptors (EGFR, TNFRSF1A, TNFRSF1B and IGF1R) (**Figure 4c**). Finally, uMs also  
318 expressed immunoregulatory genes (IL10, LGALS9, TREM2) that could enhance anti-  
319 inflammatory responses in the proliferative phase endometrium required for the characteristic  
320 scarless regeneration of this tissue (**Figure 4c**).  
321

322 Additionally, angiogenesis is also critical for tissue repair, and macrophages are known to play  
323 a role in this process<sup>53</sup>. In the endometrium, there is a profound growth of blood vessels during  
324 the proliferative phase as the *functionalis* regenerates and thickens after being shed. During  
325 the secretory phase, the vasculature further matures and coils in preparation for pregnancy.  
326 To investigate the potential interplay between uMs and the vasculature, we first defined the  
327 endometrial vascular niche. We identified three subsets of endothelial cells (venous, arterial  
328 and lymphatic) and three subsets of endometrial PV cells (ePV-1a expressing *STEAP4*, ePV-  
329 1b expressing *STC2*, and ePV-2 expressing *MMP11*) (**Supplementary Figure 6g-h**). ePV-2  
330 exhibited transcriptomic similarities to endometrial stromal cells, suggesting a transitional  
331 population between PV and stromal cells (**Supplementary Figure 1c**).  
332

333 Cell-cell communication analyses predicted signalling between the vasculature and uMs, and  
334 to a lesser extent also with uNK1 cells. Endothelial cells and ePV-1s expressed multiple  
335 extracellular matrix proteins (ECM) and cytokines (*CCL14*, *CCL23*, *CCL26*), which potentially  
336 could act to recruit innate immune cells (**Supplementary Figure 7b**). Additionally, PVs  
337 expressed *CSF1* (major macrophage growth factor), which could create a favourable  
338 environment for macrophages, stimulating their differentiation and function. In turn, uMs  
339 expressed multiple growth factor members of the pro-angiogenic VEGF family (*VEGFA*,  
340 *VEGFB*, *PIGF*), and vascular remodelling factors (*TNF*<sup>54</sup>, *OSM*<sup>55</sup>, *CXCL8*<sup>56</sup>), whose cognate  
341 receptors (*NRP1*, *NRP2*, *FLT1*, *TNFRSF1A-B*, *OSMR*, *LIFR*, *ACKR1*) were expressed by the  
342 endothelial cells (**Figure 4e, Supplementary Figure 7b**). Among the innate lymphocytes,  
343 uNK1 was the only cell subset that expressed pro-angiogenic factors (*VEGFB* and *PIGF*),  
344 although at lower levels than uterine macrophages (**Figure 4e**).  
345

346 Altogether, our analysis underscored macrophages as the major endometrial immune cells  
347 participating in the process of blood vessel formation, wound healing and anti-inflammatory  
348 responses (**Figure 4f-g**). The latter two processes are likely to aid the stromal cells in healing  
349 without scarring.  
350

351 Altered stromal-immune cell homeostasis in the eutopic endometrium of  
352 endometriosis cases

353 We next investigated whether cellular composition of the endometrium differs between  
354 endometriosis cases and controls during natural menstrual cycles, as we did not detect any  
355 endometriosis-specific cell types. After accounting for menstrual cycle phase (**see Methods**),  
356 differential abundance analysis of our nuclei dataset revealed lower abundance of  
357 decidualised stromal cells (dStromal mid) and higher abundance of uM1 macrophages in  
358 endometriosis cases (**Figure 5a**). Interestingly, decidualised stromal cells (dStromal early and  
359 dStromal mid) and macrophages (uM1 and uM2) were also identified as the top cell types  
360 enriched for the expression of genes positionally close to endometriosis risk variants when  
361 performing functional GWAS (fGWAS) analysis across the HECA cell types (**Figure 5b, see**  
362 **Methods**). The fGWAS analysis provided, for the first time, cellular context to a large-scale  
363 endometriosis GWAS meta-analysis<sup>30</sup>  
364

365 To further explore the four cell populations identified as endometriosis-relevant, we performed  
366 differential gene expression analyses between controls and endometriosis cases. In the  
367 stromal compartment of endometriosis cases, we observed changes in gene expression that

368 are likely to alter the WNT and insulin signalling pathways (**Figure 5c**). Specifically, *GREB1*  
369 (a GWAS-linked gene induced by WNT signalling<sup>57,58</sup>) was significantly upregulated, while  
370 *DKK1* (WNT inhibitor) was significantly downregulated in both dStromal early and dStromal  
371 mid cells in endometriosis. These changes suggested sustained WNT signalling in the  
372 secretory phase endometrium of donors with endometriosis. Similarly, we observed a  
373 dysregulation of insulin growth factors *IGF1* (a GWAS-linked gene) and *IGF2*. In dStromal  
374 early and dStromal mid populations, *IGF1* was significantly upregulated, while *IGF2* was  
375 significantly downregulated in endometriosis cases. *IGF1* and *IGF2* play a role in cell  
376 proliferation and differentiation<sup>59,60</sup>, suggesting dysregulation of these processes may occur in  
377 endometriosis. In the macrophage compartment, and in line with previous reports in mice<sup>61</sup>,  
378 we observed a significant upregulation of *IGF1* in uM2 of endometriosis cases (**Figure 5d**). In  
379 the uM1 population, a significant increase in expression of inflammatory genes (*TNFRSF1B*,  
380 *CEBPD*) was detected in endometriosis, in keeping with previous reports of increased  
381 inflammation in endometriosis<sup>62,63</sup>.

382  
383 Taken together, the identified shifts in cell abundance, disease-relevant populations through  
384 fGWAS and differential gene expression analyses suggest dysregulation of stromal-immune  
385 cell homeostasis in endometriosis.

## 386 Discussion

387 Globally, millions of women are affected by endometrial/uterine disorders<sup>22–24,64</sup>, yet the  
388 endometrium and the role of its cellular heterogeneity in these pathologies have been hugely  
389 understudied compared to other human tissues and diseases<sup>65</sup>. In this study, we present the  
390 HECA: the most comprehensive cellular atlas of the human endometrium assembled for  
391 individuals with/without endometriosis so far. The HECA provides a crucial step towards  
392 improving our understanding of endometrial cell heterogeneity in health and disease as it: (a)  
393 incorporates a large number of cells and individuals, (b) presents data-driven consensus cell  
394 annotation across multiple studies, (c) provides a platform for easy and rapid annotation of  
395 future scRNA-seq studies of the endometrium, and (d) enables the contextualisation of genetic  
396 association screens for endometrial/uterine disorders.

397  
398 By comprehensively analysing ~614,000 high-quality cells and nuclei from 121 individuals, we  
399 substantially surpassed the number of donors and cells profiled by the initial, pioneering  
400 endometrial single-cell studies<sup>14–21</sup>. Having such a large sample size enabled us to identify  
401 previously unreported cell states, including a relatively rare population of *CDH2+* (i.e. N-  
402 cadherin) epithelial cells. This population's marker gene expression<sup>9,34,35</sup>, localisation within  
403 the *basalis* glands, and predicted cell-cell communication with a *basalis* fibroblast population  
404 via the *CXCR4/CXCL12* axis<sup>36</sup>, strongly indicated that these cells are the previously described  
405 epithelial stem/progenitor cells. Defining the transcriptomic profile of these cells opens up new  
406 avenues for exploring their role in endometrial repair and regeneration, as well as disease  
407 pathophysiology. Functional and single-cell studies that deeply characterise the seldomly  
408 sampled *basalis* layer of the endometrium (where these rare cells reside and are reported to  
409 be a heterogeneous population<sup>2</sup>) are now warranted in a larger number of individuals.

410  
411 The HECA provides the most granular endometrial cell state annotation to date, including their  
412 spatial location *in situ*. Such spatial mapping was crucial for inferring the regulation and  
413 function of these cells given the spatiotemporal complexity of the endometrium. We captured

414 multiple novel transitory cell states (e.g. preLuminal, preGlandular, subsets of decidualised  
415 stromal cells) during the early/mid secretory phase - a period crucial for endometrial receptivity  
416 preparation in response to rising progesterone levels. A tightly regulated cellular response to  
417 the changing levels of oestrogen and progesterone is essential for menstrual cycle  
418 progression, maintenance of tissue homeostasis and fertility. Thus, the newly identified cell  
419 states could present promising targets for therapy in endometrial/uterine disorders that are  
420 characterised by the disruption of hormone-dependent downstream signalling and cellular  
421 responses<sup>66</sup>.

422  
423 Additionally, local paracrine factors and cellular crosstalk are essential for menstrual cycle  
424 progression and we provided a detailed account (and an interactive platform) of the predicted  
425 in vivo cell-cell communication across the cycle. This is an important addition to the body of  
426 existing knowledge predominantly derived from in vitro cell cultures<sup>67-69</sup>. Of particular interest  
427 is how TGF $\beta$  activity is controlled by various epithelial and mesenchymal cell states in both  
428 space and time. TGF $\beta$  signalling is known to suppress the activity of matrix  
429 metalloproteinases<sup>70,71</sup>, which are key to initiating endometrial shedding. The observed  
430 reduction in TGF $\beta$  signalling during the mid- to late secretory phase could suggest a  
431 mechanism for preparing the endometrium for shedding, or embryo implantation, and requires  
432 further studies. Interestingly, the identification and detailed description of in vivo signalling  
433 pathways involved in menstrual cycle progression could be used to refine the media used for  
434 in vitro culture of endometrial cells. For example, endometrial organoids are cultured in media  
435 supplemented with TGF $\beta$  inhibitors<sup>72,73</sup>, even when they are treated with hormones to mimic  
436 the menstrual cycle. Incorporating the spatial and temporal TGF $\beta$  signalling could help  
437 improve the physiological response and differentiation of these cells during the hormonal  
438 treatment, and thus eliminate some of the previously observed differences between in vivo  
439 and in vitro endometrial cells<sup>15</sup>.

440  
441 We also revealed a range of novel interactions by which uM may aid the process of scarless  
442 endometrial regeneration, supporting previous research that proposed a role for uM in this  
443 process<sup>74-76</sup>. The new interactions we found pinpoint uMs pivotal roles in enhancing wound  
444 healing, boosting cellular proliferation, modulating inflammation, and stimulating  
445 angiogenesis. We also discovered that uNK1, a subset of resident NK cells which we identified  
446 to increase in proportion during the secretory phase, also expressed some angiogenic  
447 molecules, although to a lesser degree than uMs. This suggests that uMs may take on a larger  
448 role than uNKs in endometrial regeneration and angiogenesis in the non-pregnant  
449 endometrium. Interestingly, interactions between uMs and stromal cells became more evident  
450 during menstruation, emphasising the crucial role that uMs play during this phase of the  
451 cycle<sup>77</sup>. Understanding how the disruption of these macrophage-stromal interactions  
452 contribute to widely common menstrual disorders (e.g. abnormal uterine bleeding) could pave  
453 new paths for the development of immunology-based treatment.

454  
455 Lastly, we demonstrated the utility of HECA to give cellular context to a large-scale  
456 endometriosis GWAS meta-analysis<sup>30</sup>. We identified two subtypes of decidualised stromal  
457 cells and macrophages as endometriosis-relevant. The observed dysregulation of stromal-  
458 immune cell homeostasis is in line with previous reports<sup>16,20,28,29,78</sup>, but overall, findings have  
459 been inconsistent. For example, some studies reported an increase in stromal cells in  
460 endometriosis cases, while others reported no changes. At the molecular level, our data  
461 indicated sustained WNT and dysregulated insulin signalling to be a feature of the dStromal

462 early/mid populations in endometriosis cases. This is in line with previous observation of  
463 downregulation of *IGF2* and lack of WNT inhibition in the endometrium of women with  
464 endometriosis during the secretory phase<sup>79-81</sup>. At the cellular level, we previously showed that  
465 inhibition of WNT signalling by stromal cells in response to progesterone is crucial in  
466 supporting the differentiation of glandular epithelium<sup>15</sup>. Our current findings suggest that this  
467 process may be disrupted in endometriosis. Yet, the observed differences were subtle (i.e.  
468 exhibited small fold changes between cases and controls), requiring further validation in a  
469 larger set of samples with detailed metadata and menstrual phase annotation. To dissect the  
470 molecular pathways and validate the involvement of WNT and insulin pathways in  
471 progesterone-mediated cellular responses could now be tested using 3D in vitro models of the  
472 endometrium encompassing both stromal and epithelial cells<sup>82</sup>.

473

474 The HECA is a key stepping stone towards the generation of a future pan-endometrial atlas  
475 encompassing endometrial cellular heterogeneity across the lifespan and in diseases. We  
476 envision a number of endometrial/uterine atlases will be generated in the coming years, and  
477 that the HECA will guide dataset integration, cell annotation and ensure reproducibility across  
478 studies. Incorporation of datasets profiling biopsies from late secretory, peri-menstrual,  
479 menstrual and generally more finely assigned menstrual cycle phases will enrich the atlas and  
480 further improve its quality. As the atlas grows both in the number of cells and individuals  
481 profiled, it will become possible to not only look at cellular variation, but also variation at the  
482 level of individuals and link genotype to phenotype. To do so, detailed and standardised  
483 phenotypic data about the individuals studied will need to be collected (e.g. BMI, race/ethnicity,  
484 fertility status, regularity of menstrual cycles) as these factors could influence the  
485 transcriptomic profile of endometrial cells and need to be evaluated.

486

487 In summary, the HECA is the first large-scale integrated reference atlas of the human  
488 endometrium, providing a conceptual framework upon which future studies can be built. With  
489 all resources publicly available in an easy-to-access interactive format, the HECA offers a  
490 platform/tool for advancing research into endometrial physiology and disorders, as well as  
491 guiding the development of physiologically-relevant in vitro model systems of the  
492 endometrium.

493

494

## 495 **Methods**

### 496 **Patient samples**

497 Superficial endometrial samples collected for the Mareckova *et al.* dataset came from four  
498 studies: (i) Endometriosis Oxford (ENDOX), (ii) Fibroids and Endometriosis Oxford (FENOX),  
499 (iii) Sanger Human Cell Atlasing Project, and (iv) Immunology and Subfertility study. Both  
500 ENDOX (REC: 09/H0604/58) and FENOX (REC: 17/SC/0664) obtained ethical approvals from  
501 the Central University Research Ethics Committee, University of Oxford. Yorkshire & The  
502 Humber - Leeds East Research Ethics Committee approved the Sanger Human Cell Atlasing  
503 Project (REC: 19/YH/0441). The Immunology of Subfertility study (REC: 08/H0606/94) was  
504 approved by the Oxford Research Ethics Committee C. In all instances, written informed  
505 consent was provided by study participants prior to obtaining tissue samples and phenotypic  
506 data.

507

508 Full-thickness uterine wall samples were obtained from deceased transplant organ donors  
509 after ethical approval (REC: 15/EE/0152, East of England–Cambridge South Research Ethics  
510 Committee) and informed consent from the donor families. Uterus was removed within 1 h of  
511 circulatory arrest.

## 512 Donor inclusion/exclusion criteria and endometriosis presence evaluation

513 Only individuals during their reproductive years were recruited and only considered having  
514 'natural cycles' if they had not taken any hormonal treatment at least 3 months prior to sample  
515 collection. Donors with endometrial cancer were excluded. In addition, we aimed to exclude  
516 patients with other benign uterine/endometrial pathologies (i.e. fibroids, polyps, adenomyosis,  
517 hyperplasia). However, in some cases ( $n = 15$ ), later histological evaluations revealed the  
518 presence of these pathologies (Supplementary Table 1). Patients taking part in the ENDOX  
519 and FENOX studies ( $n = 69$ ) were undergoing laparoscopic surgery for suspected  
520 endometriosis or infertility reasons at the John Radcliffe Hospital, Oxford. At the beginning of  
521 surgery, a pipelle biopsy of the endometrium was taken and the presence/absence of  
522 endometriosis, including endometriosis stage (rASRM stages I-IV) assigned upon surgical  
523 evaluation during the laparoscopy. Four additional control samples (i.e. samples from donors  
524 without endometriosis) came from the Sanger Cell Atlasing Project study ( $n = 3$ ) and  
525 Immunology of Subfertility study ( $n = 1$ ). Absence of endometriosis was determined based on  
526 the clinical and medical history of the patients. For the Sanger Cell Atlasing Project, patients  
527 attended a coil clinic for contraceptive reasons. During the coil insertion procedure, a biopsy  
528 of the endometrium was taken in an outpatient setting. For the Immunology and Subfertility  
529 study, patients were undergoing *in vitro* fertilisation and an endometrial biopsy was taken in  
530 an outpatient setting one cycle before the patient became pregnant and had a live birth.

## 531 Tissue processing

532 Superficial biopsies of the endometrium were collected using the Pipelle® sampling device and  
533 immediately transferred into ice-cold phosphate buffered saline (PBS) solution (Gibco,  
534 10010023). The endometrial tissue was then cut into smaller pieces and either moved into a  
535 cryovial and snap-frozen on dry ice (for single-nuclei extraction and processing) or moved into  
536 ice-cold HypoThermosol®FRS solution (Sigma-Aldrich, H4416) and stored at 4°C until further  
537 processing (either to be digested fresh or cryopreserved and digested later for single-cell  
538 processing). Where possible and sample size allowed, a small piece of tissue was also  
539 embedded in optimal cutting temperature (OCT) compound (ThermoFisher Scientific,  
540 23730571) inside a cryomold and rapidly frozen in dry ice/isopentane slurry for histological  
541 evaluation and analyses.

542

543 Whole uterus samples used for single-cell RNA-sequencing and imaging analyses were stored  
544 in *HypoThermosol®FRS* at 4°C until processing. For imaging analyses, the samples were  
545 further dissected, embedded in OCT media and rapidly frozen in dry ice/isopentane slurry.  
546 For single-cell RNA-sequencing (donor A70), to enrich endometrial cells, the endometrium  
547 was excised from the myometrium using scalpels and digested as detailed below.

548 Tissue cryopreservation

549 Fresh tissue was cut into <1 mm<sup>3</sup> segments before being resuspended with 1 ml of ice cold  
550 Cryostor solution (CS10) (C2874-Sigma). The tissue was frozen at -80°C decreasing the  
551 temperature approximately 1°C per minute. Detailed protocol available at  
552 <https://www.protocols.io/view/tissue-freezing-in-cryostor-solution-processing-bgsnjwde>.

553 Tissue dissociation for single-cell RNA-sequencing

554 Cryopreserved samples were thawed at 37°C, quickly transferred to a 15 ml tube and topped-  
555 up with 13 ml of ice cold RPMI/FBS. Samples were centrifuged (500 x g, 5 min, 4°C) and the  
556 supernatant discarded. The tissue was enzymatically digested on a MACSMix rotator (set to  
557 16 rpm speed) at 37°C in pre-warmed RPMI/FBS containing Collagenase V (Sigma-Aldrich,  
558 C9263), and DNase I (Roche, 11284932001) with final concentrations of 1 mg/ml and 0.1  
559 mg/ml, respectively. Digested tissue was centrifuged (500 x g, 5 min), resuspended in 10 ml  
560 of PBS and passed through a 40 µm cell strainer (BD Biosciences, 352340), generating the  
561 collagenase fraction, enriched in stromal and immune cells (Figure 3.1). The filter was back-  
562 washed with PBS into a 50 ml tube and centrifuged (500 x g, 5 min). Supernatant was  
563 discarded and any undigested tissue within the pellet was incubated with 0.25% (v/v) trypsin-  
564 EDTA (Sigma-Aldrich, T3924) and DNase I (0.1 mg/ml) at 37°C for 15 min on a MACSMix  
565 rotator. The digestion process was stopped by adding RPMI/FBS and samples centrifuged  
566 (500 x g, 5 min). This step yielded the trypsin fraction. The collagenase fraction was  
567 centrifuged (500 x g, 5 min) and resuspended in 2 ml of red-blood-cell (RBC) lysis buffer  
568 (eBioscience, 00-4300) for 5-10 min at room temperature. After incubation, the samples were  
569 centrifuged (500 x g, 5 min), the RBC buffer discarded and both fractions (collagenase and  
570 trypsin) resuspended in 0.04% bovine serum albumin (BSA) (Sigma-Aldrich, A9418) in PBS  
571 (v/v). The generated single-cell suspensions were stored on ice and counted before being  
572 loaded separately onto the 10x Chromium chip.

573

574 In the case of two samples (donor IDs: FX1125 and FX1176), cells from the collagenase  
575 fraction were live/dead sorted prior to loading to enrich for live cells. The nuclear stain DAPI  
576 (4',6-diamidino-2-phenylindole) was used to visualise and distinguish live/dead cells and  
577 debris.

578 Tissue dissociation for single-nucleus RNA-sequencing

579 Snap-frozen endometrial pipelle biopsies were removed from cryovials and embedded in OCT  
580 for cryosectioning, storing them at -80°C overnight. The following day, the OCT blocks were  
581 left inside the cryostat for ~1 h to equilibrate to the chamber temperature of -20°C. The blocks  
582 were trimmed until reaching the tissue, when the first 10 µm thick sections for morphological  
583 assessment under a light microscope started to be collected. Three sections were placed on  
584 SuperFrost® Plus slides (ThermoFisher, 12312148) before cutting and collecting 50 µm thick  
585 sections for nuclei extraction. Depending on tissue size, between 10 to 20 sections were  
586 placed into a 7 ml Dounce tissue grinder (Sigma-Aldrich, D9063-1SET) on dry-ice and a further  
587 three 10 µm thick sections were placed on slides and stored at -80°C for later histological  
588 staining.

589

590 Tissue collected in the Dounce tissue grinder was placed on ice inside a class II safety cabinet  
591 and incubated with 3 ml of homogenisation buffer (see Supplementary Table 5 for buffer  
592 composition) for 5 min. To help dissolve the OCT, the suspension was gently mixed with a 2  
593 ml aspiration pipette half-way through the incubation. The tissue was then homogenised by  
594 10-20 strokes of both pestle A and B. The number of strokes was sample-dependent -  
595 homogenisation with each pestle was performed until no resistance and tissue changes were  
596 observed. Each pestle was washed with 500  $\mu$ l of the homogenisation buffer and the  
597 homogenate filtered through a 40  $\mu$ m cell strainer into a new 50 ml tube. The sample was then  
598 centrifuged using the following setting: 500 x g, 6 min, 4°C, acceleration set at 0 and  
599 deceleration set to 3. After removing the supernatant, 500  $\mu$ l of wash buffer (see  
600 Supplementary Table 6 for buffer composition) was added to the cell pellet and incubated for  
601 2 min on ice. The nuclei pellet was gently resuspended using wide-bore tips to avoid damaging  
602 the nuclei, and the yield checked using a haemocytometer and trypan blue. Next, the nuclei  
603 suspension was transferred to a 1.5 ml tube and washed twice by adding 1 ml of the wash  
604 buffer and centrifugation (500 x g, 3 min, 4°C). The supernatant was removed and nuclei  
605 resuspended in 200  $\mu$ l of the wash buffer (volume was nuclei yield-dependent). To remove  
606 debris and clumps, the nuclei suspension was filtered twice through the 40  $\mu$ m Flowmi® cell  
607 strainers and nuclei counted using a haemocytometer and trypan blue. The nuclei suspension  
608 were stored on ice until loading the 10x Chromium chip.

#### 609 Assignment of menstrual stage

610 OCT blocks were sectioned at 10  $\mu$ M thickness and haematoxylin and eosin-stained following  
611 standard protocols. Menstrual phase was assigned based on histological evaluation by two  
612 independent pathologists. Where this was not possible, the menstrual phase was assigned  
613 based on the transcriptomic data and cellular profiles of the samples (see Supplementary  
614 Table 1).

#### 615 Donor genotyping

616 Buffy coats of 33 participants were genotyped using Illumina Global Screening Array (GSA)  
617 v3 with remaining genotypes retrieved from prior genotyping rounds using Affymetrix Precision  
618 Medicine Array (9 samples, including 5 in overlap with GSA v3), and Affymetrix Axiom (4  
619 samples, 2 in overlap with Precision Medicine Array). Samples and variants quality was  
620 assessed using standard protocol<sup>83</sup>. Four samples were flagged (2 due to divergent ancestry,  
621 2 due to low genotyping rate), two of which were re-genotyped on GSA v3. Variants passing  
622 QC (49.5% for Affymetrix arrays, 76.7% for GSA) were lifted from hg19 reference to GRCh38  
623 using pyliftover and UCSC chain (v2013-12-31) with 99.92% success rate. The lifted SNPs  
624 were aligned to GRCh38.p13 reference using plink2<sup>84</sup> and exported to VCF. Stand issues  
625 arising from ambiguous plink1 source data were fixed using bcftools<sup>85</sup> against GRCh38.p13  
626 reference (<5% flipped).

#### 627 Haematoxylin and Eosin (H&E) staining and imaging

628 Fresh frozen sections were removed from -80°C storage and air dried before being fixed in  
629 10% neutral buffered formalin for 5 minutes. After rinsing with deionised water, slides were  
630 dipped in Mayer's Haematoxylin solution for 90 seconds. Slides were completely rinsed in 4-  
631 5 washes of deionised water, which also served to blue the haematoxylin. Aqueous eosin (1%)

632 was manually applied onto sections with a pipette and rinsed with deionised water after 1-3  
633 seconds. Slides were dehydrated through an ethanol series (70%, 70%, 100%, 100%) and  
634 cleared twice in 100% xylene. Slides were coverslipped and allowed to air dry before being  
635 imaged on a Hamamatsu Nanozoomer 2.0HT digital slide scanner.

636 Multiplexed smFISH and high-resolution imaging

637 Large tissue section staining and fluorescent imaging was conducted largely as described  
638 previously<sup>86</sup>. Sections were cut from fresh frozen embedded in OCT at a thickness of 10 µm  
639 using a cryostat, placed onto SuperFrost Plus slides (VWR) and stored at -80°C until stained.  
640 Tissue sections were then processed using a Leica BOND RX to automate staining with the  
641 RNAscope Multiplex Fluorescent Reagent Kit v2 Assay (Advanced Cell Diagnostics, Bio-  
642 Techne), according to the manufacturers' instructions. Probes used are found in  
643 Supplementary Table 7. Prior to staining, tissue sections were post-fixed in 4%  
644 paraformaldehyde in PBS for 15 minutes at 4°C, then dehydrated through a series of 50%,  
645 70%, 100%, and 100% ethanol, for 5 minutes each. Following manual pre-treatment,  
646 automated processing included epitope retrieval by protease digestion with Protease IV for 30  
647 minutes prior to probe hybridisation. Tyramide signal amplification with Opal 520, Opal 570,  
648 and Opal 650 (Akoya Biosciences) and TSA-biotin (TSA Plus Biotin Kit, Perkin Elmer) and  
649 streptavidin-conjugated Atto 425 (Sigma Aldrich) was used to develop RNAscope probe  
650 channels. Stained sections were imaged with a Perkin Elmer Opera Phenix High-Content  
651 Screening System, in confocal mode with 1 µm z-step size, using a 20X (NA 0.16, 0.299  
652 µm/pixel); 40X (NA 1.1, 0.149 µm/pixel); water-immersion objective. Channels: DAPI  
653 (excitation 375 nm, emission 435-480 nm), Atto 425 (ex. 425 nm, em. 463-501 nm), Opal 520  
654 (ex. 488 nm, em. 500-550 nm), Opal 570 (ex. 561 nm, em. 570-630 nm), Opal 650 (ex. 640  
655 nm, em. 650-760 nm). *Image stitching*: Confocal image stacks were stitched as two-  
656 dimensional maximum intensity projections using proprietary Acapella scripts provided by  
657 Perkin Elmer.

658 10x Genomics Chromium GEX library preparation and sequencing

659 Both cells and nuclei undergoing scRNA-seq and snRNA-seq were loaded according to the  
660 manufacturer's protocol for the Chromium Single Cell 3' Kit v.3.0, and v3.1 (10X Genomics) to  
661 attain between 2,000 and 10,000 cells/nuclei per reaction. Libraries were sequenced, aiming  
662 at a minimum coverage of 50,000 raw reads per cell, on the Illumina Novaseq 6000 system;  
663 using the sequencing format; read 1: 28 cycles; i7 index: 10 cycles, i5 index: 10 cycles; read  
664 2: 90 cycles.

665 10x Genomics Visium library preparation and sequencing

666 We generated 10x Genomics Visium transcriptomic slides from two superficial biopsies.  
667 Briefly, 10 micron cryosections were cut and placed on Visium slides v1 3'. These were  
668 processed according to the manufacturer's instructions. Briefly, sections were fixed with cold  
669 methanol, stained with haematoxylin and eosin and imaged on a Hamamatsu NanoZoomer  
670 S60 before permeabilisation, reverse transcription and cDNA synthesis using a template-  
671 switching protocol. Second-strand cDNA was liberated from the slide and single-indexed  
672 libraries prepared using a 10x Genomics PCR-based protocol. Libraries were pooled and

673 sequenced on a Novaseq 6000), with the following sequencing format; read 1: 28 cycles, i7  
674 index: 10 cycles, i5 index: 10 cycles and read 2: 90 cycles.

## 675 External human endometrial scRNA-seq and Visium datasets

676 We collected raw sequencing data from previously published human endometrial scRNA-seq  
677 datasets. Specifically, we downloaded publicly available .fastq files either from Gene  
678 Expression Omnibus (GEO) or ArrayExpress. These datasets included: (i) Wang et al. (GEO  
679 accession number GSE111976), (ii) Garcia-Alonso et al. (ArrayExpress accession number E-  
680 MTAB-10287), (iii) Tan et al. (GEO accession number GSE179640), (iv) Lai et al. (GEO  
681 accession number GSE183837), (v) Fonseca et al. (GEO accession number GSE213216), and  
682 (vi) Huang et al. (GEO accession number GSE214411).

683

684 For spatial transcriptomics analysis, we used the 10x Genomics Visium from two full thickness  
685 uterus previously generated by us, available at ArrayExpress (accession number E-MTAB-  
686 9260).

## 687 Alignment and quantification of sc/snRNA-seq data

688 Reads from both the newly generated scRNA-seq/snRNA-seq libraries and external datasets  
689 were alignment to the 10x Genomics' human reference genome GRCh38-2020-A, followed by  
690 cell calling, transcript quantification and quality control (QC) using the Cell Ranger Software  
691 (version 6.0.2; 10X Genomics) with default parameters. Cell Ranger filtered count matrices  
692 were used for downstream analysis.

## 693 Downstream sc/snRNA-seq analysis

### 694 Donor demultiplexing and doublet identification

695 For 84 of the newly generated libraries (26 in the scRNA-seq and 58 in the snRNA-seq  
696 datasets) we multiplexed cell suspensions from two different donors. To ensure that we could  
697 confidently assign cells back to their donor, we genotyped some donors as described in the  
698 *Donor genotyping* section above, and then pooled sample combinations in a way that each  
699 scRNA-seq/snRNA-seq library contained at least one genotyped donor.

700

701 To assign each cell/nuclei in the scRNA-seq/snRNA-seq libraries back to their donor-of-origin,  
702 we genotyped each barcode. Specifically, we called the SNPs in the reads from each barcode  
703 and piled them up using the cellSNP tool v1.2.2. Here, reads were genotyped from the Cell  
704 Ranger BAM files using a reference list of human common variants from the 1000 Genome  
705 Project (hg38 version with minor allele frequency (MAF) > 0.0005) that we downloaded from  
706 <https://sourceforge.net/projects/cellsnp/files/SNPlist>. Once the cells in scRNA-seq/snRNA-  
707 seq libraries were genotyped, we linked them back to their donor-of-origin genotype (obtained  
708 using Illumina Global Array) using vireoSNP v0.5.8 with default parameters (n\_donor = 2).  
709 Barcodes classified as either "doublet" (i.e. containing the two genotypes) or "unassigned"  
710 were discarded in downstream analysis.

711 Doublet detection based on transcriptional mixtures

712 We quantified cell-doublet likelihood for each barcode with Scrublet software on a per-library  
713 basis. We used a two-step diffusion doublet identification followed by Bonferroni-FDR  
714 correction and a significance threshold of 0.01, as described in<sup>87</sup>. Barcodes estimated as  
715 doublets were not excluded from the initial analysis, instead these were kept in the  
716 downstream analysis and used to identify doublet-enriched clusters.

717 Quality filters, batch correction and clustering

718 For both scRNA-seq and snRNA-seq libraries, we used the filtered count matrices from Cell  
719 Ranger 6.0.2 for downstream analysis and analysed them with Scanpy v.1.7.0, with the  
720 pipeline following their recommended standard practises. We applied stringent QC to further  
721 filter the cells called by Cell Ranger to retain only high-quality cells. Specifically, we excluded  
722 cells either (i) expressing fewer than 1,000 genes or (ii) with a mitochondrial content higher  
723 than 20%. For some datasets, these filters discarded more than 50% of the initial called cells.  
724

725 Next, we flagged cell-cycle genes using a data-driven approach as described in<sup>87,88</sup>. To do  
726 so, after converting the expression space to  $\log(\text{CPM}/100 + 1)$ , we transpose the object to  
727 gene space, performing PCA, neighbour identification and Leiden clustering. The gene  
728 members of the gene cluster encompassing well-known cycling genes (*CDK1*, *MKI67*, *CCNB2*  
729 and *PCNA*) were all flagged as cell cycling genes, and discarded in each downstream  
730 analysis. In parallel, we also used the scanpy function “score\_genes\_cell\_cycle” to infer the  
731 cell cycle stage of each cell (i.e. G1, G2/M or S) that was later used to interpret the clusters.  
732

733 Next, we generated an integrated manifold for scRNA-seq and snRNA-seq datasets  
734 separately. The scRNA-seq manifold included data from 6 previously published studies as well  
735 as the scRNA-seq data newly generated by us. The snRNA-seq exclusively contains newly  
736 generated data for this study. To minimise cell cycle bias, the previously flagged cell-cycle  
737 genes were excluded. The integrated manifolds were generated using single-cell Variational  
738 Inference (scVI) v0.6.8, with both the donor and study id (for scRNA-seq only) as batches. All  
739 the remaining parameters were kept as default, with *n\_latent*= 32, *n\_layers*=2. The scVI low  
740 dimensional space was estimated on the top 2,000 most highly variable genes in each dataset,  
741 which were defined using *Seurat* v3 flavour on the raw counts. With the resulting scVI-  
742 corrected latent representation of each cell, we estimated the neighbour graph, generated a  
743 Uniform Manifold Approximation and Projection (UMAP) visualisation and performed Leiden  
744 clustering.

745

746 The same strategy was used to zoom-in into each of the four main cell lineages (i.e. epithelial,  
747 mesenchymal, immune and endothelial) to further resolve the cellular heterogeneity in those  
748 compartments. Here, we subset the cells to those in the lineage and repeated scVI integration  
749 using the top 2,000 most highly variable genes within each lineage. The donor and the study  
750 id were kept as batches, with default parameters, *n\_latent*= 64 and *n\_layers*=2. For the zoom-  
751 in analysis into the immune compartment, donors taking exogenous hormones (Tan et al  
752 dataset) were excluded due to integration challenges.

753 Annotation of cell types

754 We performed a full re-annotation of the cell clusters in the integrated scRNA-seq manifold.  
755 First, we carried out a new quality control round to exclude clusters that are likely driven by  
756 technical artefacts (i.e. low QC cells or doublets). Briefly, we flagged as *low QC clusters* those  
757 that (i) express an overall lower number of genes, (ii) express an overall lower number of  
758 counts, (iii) display a higher than average mitochondrial or nuclear RNA content and,  
759 importantly (iv) do not express any distinctive gene (and thus are not representing any  
760 independent biological entity). Next, we flagged as *doublets* those clusters that met the  
761 following criteria (i) exhibit higher scrublet doublet score; (ii) express marker genes from  
762 multiple lineages (for example, display both epithelial and immune markers) and (iii) do not  
763 express any distinctive gene. Distinctive marker genes were identified using TF-IDF, as  
764 implemented in the *SoupX* package v.1.5.0.

765

766 To assign cell type labels to remaining high-quality clusters, we took into account the following  
767 variables: (i) the menstrual cycle phase bias (or any other clinical variable such exogenous  
768 hormones, endometriosis, etc), (ii) the expression of previously described markers, (iii) the  
769 differentially expressed genes and (iv) the spatial location, either by performing smFISH or by  
770 deconvoluting the cellular composition of Visium spots.

771

772 Because of the higher gene coverage of the scRNA-seq data, cell type identification and  
773 annotation was done primarily on the integrated scRNA-seq dataset. To annotate the snRNA-  
774 seq clusters, we trained a Support Vector Machine (SVM) classifier (*sklearn.svm.SVC*) on the  
775 scRNA-seq dataset and transferred labels onto the denoised (i.e. decontaminated of ambient  
776 RNA) snRNA-seq dataset. Denoising of snRNA-seq was done with *DecontX* from the R *celda*  
777 package v1.6.1. Predicted cell type annotations on snRNA-seq were validated or disproved  
778 by looking at the expression of marker genes.

779 Query-to-HECA mapping

780 We used the scArches model surgery framework<sup>32</sup> to project new samples onto the same  
781 latent space as single-cell HECA. The scVI model used in main analysis was trained using  
782 both dataset and sample ID as covariates. In order to build a model compatible with the  
783 scArches framework, we trained a scANVI model with only sample ID as batch covariate. We  
784 trained the reference scANVI model for 20 epochs, based on an scVI model with *n\_layers* =  
785 2. The surgery model was trained for 100 epochs with *weight\_decay*=0.0 to ensure reference  
786 cell embeddings would remain identical. To obtain joint embeddings, we concatenated gene  
787 expression counts from HECA reference cells and query samples into a single object and used  
788 the surgery encoder to get latent representations. We then computed the kNN graph (default  
789 parameters) and UMAP (*min\_dist* = 0.4) on the joint embeddings. We evaluated the quality of  
790 the query to reference mapping by examining the alignment on the UMAP and the  
791 concordance of marker gene expression in HECA reference cells and query samples.

792

793 We provide step-by-step scArches tutorials at <https://github.com/ventolab/HECA-Human->  
794 [Endometrial-Cell-Atlas/blob/main/tutorials/query\\_to\\_ref\\_mapping.ipynb](https://github.com/ventolab/HECA-Human-Endometrial-Cell-Atlas/blob/main/tutorials/query_to_ref_mapping.ipynb) to support mapping  
795 new samples to HECA reference cells based on any input gene expression count matrix.

796 Alignment and quantification of Visium data

797 The newly generated 10x Visium spatial sequencing data was processed using Space Ranger  
798 Software (v.2.0.1) to identify the spots under tissue, align reads to the 10x Genomics' human  
799 reference genome GRCh38-2020-A and quantify gene counts. Spots were automatically  
800 aligned to the paired H&E images by Space Ranger software. All spots under tissue detected  
801 by Space Ranger were included in downstream analysis.

802 Downstream analysis of Visium data

803 Location of cell types in Visium data

804 We spatially map the cell types from the scRNA-seq dataset on the Visium slides with  
805 cell2location tool v0.06-alpha<sup>89</sup>. We deconvoluted both, the Visium slides newly generated in  
806 this study from superficial biopsies and the ones downloaded from E-MTAB-9260 covering full  
807 thickness uterus. As reference, we used the cell type signatures from the scRNA-seq dataset,  
808 subsetting the cells to those expressing more than 2,000 genes. Cell2location was run with  
809 default parameters, with the exception of *cells\_per\_spot* which was set to 20. Each Visium  
810 section was analysed separately. The estimated abundance for each cell type was visualised  
811 following the *cell2location* tutorial.

812 Cell-cell communication analysis with CellPhoneDB

813 Because two cell types can only interact paracrinally or juxtacrinally if they co-localise in space  
814 and time, we first manually classified the cell types into the spatiotemporal microenvironments  
815 where these coexists (for example, endothelial and PV cells coexist in the vessels, while  
816 preGlandular coexists with dStromal early cells in the *functionalis* layer of the early secretory  
817 endometrium). Spatial location was derived from prior knowledge, smFISH experiments or cell  
818 type deconvolution of Visium spots with cell2location. The temporal location was directly  
819 derived from the menstrual phase where the cell types are detected.

820  
821 To identify paracrine or juxtacrine interactions between the cells co-localising in an  
822 endometrial microenvironment, we used the DEGs-based method of CellphoneDB v4.1<sup>90</sup>.  
823 Using this method, we retrieved interacting pairs of ligands and receptors meeting the  
824 following requirements: i) all the interacting partners were expressed by at least 10% of the  
825 cell type under consideration; ii) the interacting cell type pairs share an endometrial  
826 microenvironment and iii) at least one of the interacting partners (for example, either the ligand  
827 or the receptor) was significantly upregulated in the corresponding cell type (Wilcoxon Tests;  
828 adjusted p-value < 0.01 and a log2 fold change > 0.75). Differential expression analysis was  
829 performed on a per-lineage approach to identify the genes specifically upregulated in a cell  
830 state, compared to the other cell states in the same lineage. Donors under exogenous  
831 hormonal therapy were excluded from the analysis.

832 Differential cell abundance (DCA)

833 To quantify changes in cellular composition, we used differential abundance analysis on cell  
834 neighbourhoods with RMilo v1.6.0<sup>91</sup>.

836 To evaluate compositional changes of immune cells between the proliferative or the secretory  
837 phases of the menstrual cycle, we first calculated the KNN graph derived from the scVI  
838 immune-embedding subsetted to contain only superficial biopsies from controls (excluding  
839 donors under exogenous hormone therapy). Next, we assigned cells to neighbourhoods and  
840 counted the number of cells belonging to each cell type in each neighbourhood. We assigned  
841 each neighbourhood to a cell type label based on majority voting of the cells belonging to that  
842 neighbourhood. Cell neighbourhoods where less than 70% of cells came from a single cell  
843 type were labelled as “Mixed neighbourhoods” and discarded. To test for differential  
844 abundance across the menstrual cycle, we divided the samples into proliferative and the  
845 secretory phases. RMilo models the cell count in neighbourhoods as a negative binomial  
846 generalised linear model, using a log-linear model to model the effects of menstrual phase on  
847 cell counts, while accounting for the total number of cells over all the neighbourhoods. When  
848 analysing the scRNA-seq dataset, we also included the study id as covariate of the model to  
849 account for the variability between laboratory/technical batches. A neighbourhood was  
850 associated with the proliferative phase if  $\text{SpatialFDR} < 0.1$  and  $\text{logFC} < 0$ , or the secretory  
851 phase if  $\text{SpatialFDR} < 0.1$ ,  $\text{logFC} > 0$ . The analysis was performed primarily with the snRNA-  
852 seq datasets to minimise laboratory bias, and validated on the scRNA-seq dataset where we  
853 included the study id as model covariate.

854

855 To evaluate compositional changes of mesenchymal, epithelial, endothelial and immune cells  
856 between endometriosis and controls, we again relied on the KNN graph derived from the scVI  
857 lineage-subanalysis embedding. Nuclei were subsetted to those coming only from superficial  
858 biopsies, excluding donors under exogenous hormone therapy. Following the strategy  
859 described above, we estimated differential abundance between control and endometriosis  
860 case samples using the snRNA-seq dataset, as it has an even coverage of cases and controls  
861 along the menstrual cycle and avoids laboratory bias. Stromal and epithelial populations are  
862 menstrual-phase specific, and were tested considering donors in the corresponding phase.  
863 For testing differences in immune cells we instead added the menstrual phase as a covariate  
864 in the model. A neighbourhood was associated with control samples if  $\text{SpatialFDR} < 0.1$  and  
865  $\text{logFC} < 0$ , or endometriosis case samples if  $\text{SpatialFDR} < 0.1$ ,  $\text{logFC} > 0$ .

## 866 Cell type enrichment analysis for Endometriosis-GWAS genes

867 To study the association between the endometrial cell populations in our atlas and previously  
868 identified endometriosis GWAS loci, we used the functional GWAS (fGWAS) approach  
869 described in<sup>92</sup>. This approach evaluates the enrichment of various functional annotations for  
870 molecular quantitative traits (in this case, the gene expression signature of a cell type) and  
871 GWAS loci (in this case, the cis-regulatory variants associated with endometriosis). Here,  
872 genetic variants were linked to genes if they map to their cis-regulatory region, which is defined  
873 as  $\pm 500$  Kb centred at the transcription start site (TSS) of the gene. The association statistics  
874 (the log odds ratios and standard errors) were transformed into the approximate Bayes factors  
875 using the Wakefield method<sup>92,93</sup>. The Bayes factors of variants mapping to each gene cis-  
876 regulatory region were weighted and averaged by the prior probability, estimated as the  
877 exponential function to TSS proximity. Finally, the enrichment of each cell type was estimated  
878 as the maximum likelihood estimator of the effect size for the cell-type-specific expression.

879

880 Endometriosis GWAS loci were derived from the full summary statistics of our recent  
881 endometriosis GWAS meta-analysis<sup>30,94</sup> excluding the 23andMe dataset. The full summary

882 statistics, indicating the SNP position, beta value and standard error used to perform the  
883 fGWAS analysis, are publicly available from EBI GWAS Catalog (GCST90205183).

## 884 Differential gene expression endometriosis vs controls

885 We evaluated the magnitude and significance of the differences in gene expression between  
886 endometriosis patients and controls using limma v.3.54.2. First, to avoid unwanted  
887 confounding effects, we subsetted the data to contain only superficial biopsies and excluded  
888 donors under exogenous hormonal therapy. Secondly, to account for within-sample  
889 correlations (i.e. cells coming from the same donor), pseudobulking with sum aggregation was  
890 performed prior to applying limma. Briefly, we generated 3 pseudobulks per donor and per cell  
891 type by aggregating the cells of each cell type and taking the mean gene expression within  
892 the cell type. Finally, we tested for differential expression between conditions (endometriosis  
893 vs control) using the limma-voom approach. The analysis was performed on the scRNA-seq  
894 datasets, and we reported as differentially expressed genes with FDR < 0.1.

## 895 Data availability

896 Datasets are available from ArrayExpress ([www.ebi.ac.uk/arrayexpress](http://www.ebi.ac.uk/arrayexpress)), with accession  
897 number pending. Multiplexed smFISH images are available from BioStudies  
898 ([www.ebi.ac.uk/biostudies](http://www.ebi.ac.uk/biostudies)), with accession number pending. All data is public access. Source  
899 data are provided with this paper. scRNA-seq and snRNA-seq datasets to reproduce UMAPs  
900 and dotplots can be accessed and downloaded through the web portals  
[https://www.reproductivecellatlas.org/endometrium\\_reference.html](https://www.reproductivecellatlas.org/endometrium_reference.html).

## 902 Code availability

903 All the code used for data analysis is available at: <https://github.com/ventolab/HECA-Human->  
904 [Endometrial-Cell-Atlas](https://github.com/ventolab/HECA-Human-Endometrial-Cell-Atlas).

## 905 References

- 906 1. Critchley, H. O. D., Maybin, J. A., Armstrong, G. M. & Williams, A. R. W. Physiology of  
907 the Endometrium and Regulation of Menstruation. *Physiol. Rev.* (2020)  
908 doi:10.1152/physrev.00031.2019.
- 909 2. Salamonsen, L. A., Hutchison, J. C. & Gargett, C. E. Cyclical endometrial repair and  
910 regeneration. *Development* **148**, dev199577 (2021).
- 911 3. Tempest, N. *et al.* Histological 3D reconstruction and in vivo lineage tracing of the  
912 human endometrium. *J. Pathol.* **251**, 440–451 (2020).
- 913 4. Yamaguchi, M. *et al.* Three-dimensional understanding of the morphological complexity  
914 of the human uterine endometrium. *iScience* **24**, 102258 (2021).
- 915 5. Tempest, N. *et al.* Novel microarchitecture of human endometrial glands: implications in  
916 endometrial regeneration and pathologies. *Hum. Reprod. Update* **28**, 153–171 (2022).
- 917 6. Prianishnikov, V. A. A functional model of the structure of the epithelium of normal,

918        hyperplastic and malignant human endometrium: a review. *Gynecol. Oncol.* **6**, 420–428  
919        (1978).

920        7. Gray, C. A. *et al.* Developmental Biology of Uterine Glands. *Biol. Reprod.* **65**, 1311–  
921        1323 (2001).

922        8. Gargett, C. E., Chan, R. W. & Schwab, K. E. Endometrial stem cells. *Curr. Opin. Obstet.*  
923        *Gynecol.* **19**, (2007).

924        9. Valentijn, A. J. *et al.* SSEA-1 isolates human endometrial basal glandular epithelial cells:  
925        phenotypic and functional characterization and implications in the pathogenesis of  
926        endometriosis. *Hum. Reprod.* **28**, 2695–2708 (2013).

927        10. Tempest, N., Maclean, A. & Hapangama, D. K. Endometrial Stem Cell Markers: Current  
928        Concepts and Unresolved Questions. *Int. J. Mol. Sci.* **19**, (2018).

929        11. Male, V. & Moffett, A. Natural Killer Cells in the Human Uterine Mucosa. *Annu. Rev.*  
930        *Immunol.* (2023) doi:10.1146/annurev-immunol-102119-075119.

931        12. Monin, L., Whettlock, E. M. & Male, V. Immune responses in the human female  
932        reproductive tract. *Immunology* (2019) doi:10.1111/imm.13136.

933        13. Oreshkova, T., Dimitrov, R. & Moudjeva, M. A cross-talk of decidual stromal cells,  
934        trophoblast, and immune cells: a prerequisite for the success of pregnancy. *Am. J.*  
935        *Reprod. Immunol.* **68**, 366–373 (2012).

936        14. Wang, W. *et al.* Single-cell transcriptomic atlas of the human endometrium during the  
937        menstrual cycle. *Nat. Med.* **26**, 1644–1653 (2020).

938        15. Garcia-Alonso, L. *et al.* Mapping the temporal and spatial dynamics of the human  
939        endometrium in vivo and in vitro. *Nat. Genet.* **53**, 1698–1711 (2021).

940        16. Tan, Y. *et al.* Single-cell analysis of endometriosis reveals a coordinated transcriptional  
941        programme driving immunotolerance and angiogenesis across eutopic and ectopic  
942        tissues. *Nat. Cell Biol.* **24**, 1306–1318 (2022).

943        17. Fonseca, M. A. S. *et al.* Single-cell transcriptomic analysis of endometriosis. *Nat. Genet.*  
944        (2023) doi:10.1038/s41588-022-01254-1.

945        18. Huang, X. *et al.* Single-cell transcriptome analysis reveals endometrial immune  
946        microenvironment in minimal/mild endometriosis. *Clin. Exp. Immunol.* uxad029 (2023).

947        19. Lai, Z.-Z. *et al.* Single-cell transcriptome profiling of the human endometrium of patients  
948        with recurrent implantation failure. *Theranostics* **12**, 6527–6547 (2022).

949        20. Shih, A. J. *et al.* Single-cell analysis of menstrual endometrial tissues defines  
950        phenotypes associated with endometriosis. *BMC Med.* **20**, 315 (2022).

951        21. Queckbörner, S. *et al.* Stromal Heterogeneity in the Human Proliferative Endometrium-A  
952        Single-Cell RNA Sequencing Study. *J Pers Med* **11**, (2021).

953        22. Vannuccini, S., Jain, V., Critchley, H. & Petraglia, F. From menarche to menopause,  
954        heavy menstrual bleeding is the underrated compass in reproductive health. *Fertil.*

955         *Steril.* **118**, 625–636 (2022).

956     23. Sung, H. *et al.* Global Cancer Statistics 2020: GLOBOCAN Estimates of Incidence and  
957         Mortality Worldwide for 36 Cancers in 185 Countries. *CA Cancer J. Clin.* **71**, 209–249  
958         (2021).

959     24. Zondervan, K. T., Becker, C. M. & Missmer, S. A. Endometriosis. *N. Engl. J. Med.* **382**,  
960         1244–1256 (2020).

961     25. Nnoaham, K. E. *et al.* Impact of endometriosis on quality of life and work productivity: a  
962         multicenter study across ten countries. *Fertil. Steril.* **96**, (2011).

963     26. Prašnikar, E., Knez, J., Kovačič, B. & Kunej, T. Molecular signature of eutopic  
964         endometrium in endometriosis based on the multi-omics integrative synthesis. *J. Assist.  
965         Reprod. Genet.* **37**, 1593–1611 (2020).

966     27. Miravet-Valenciano J, Ruiz-Alonso M, Gómez E, Garcia-Velasco JA. Endometrial  
967         receptivity in eutopic endometrium in patients with endometriosis: it is not affected, and  
968         let me show you why. *Fertil. Steril.* **108**, 28–31 (2017).

969     28. Bunis, D. G. *et al.* Whole-Tissue Deconvolution and scRNASeq Analysis Identify Altered  
970         Endometrial Cellular Compositions and Functionality Associated With Endometriosis.  
971         *Front. Immunol.* **12**, 788315 (2021).

972     29. Baugh, L. *et al.* Integrating endometrial proteomic and single cell transcriptomic  
973         pipelines reveals distinct menstrual cycle and endometriosis-associated molecular  
974         profiles. *bioRxiv* (2022) doi:10.1101/2022.01.29.22269829.

975     30. Rahmioglu, N. *et al.* The genetic basis of endometriosis and comorbidity with other pain  
976         and inflammatory conditions. *Nat. Genet.* **55**, 423–436 (2023).

977     31. Liu, C. *et al.* Single-cell dissection of cellular and molecular features underlying human  
978         cervical squamous cell carcinoma initiation and progression. *Sci Adv* **9**, eadd8977  
979         (2023).

980     32. Lotfollahi, M. *et al.* Mapping single-cell data to reference atlases by transfer learning.  
981         *Nat. Biotechnol.* **40**, 121–130 (2021).

982     33. Xu, C. *et al.* Probabilistic harmonization and annotation of single-cell transcriptomics  
983         data with deep generative models. *Mol. Syst. Biol.* **17**, e9620 (2021).

984     34. Nguyen, H. P. T. *et al.* N-cadherin identifies human endometrial epithelial progenitor  
985         cells by in vitro stem cell assays. *Hum. Reprod.* **32**, 2254–2268 (2017).

986     35. Ma, S. *et al.* Expression of ALDH1A Isozymes in Human Endometrium with and without  
987         Endometriosis and in Ovarian Endometrioma. *Reprod. Sci.* **27**, 443–452 (2020).

988     36. Sugiyama, T., Kohara, H., Noda, M. & Nagasawa, T. Maintenance of the hematopoietic  
989         stem cell pool by CXCL12-CXCR4 chemokine signaling in bone marrow stromal cell  
990         niches. *Immunity* **25**, 977–988 (2006).

991     37. Qu, Y. *et al.* The dual delivery of KGF and bFGF by collagen membrane to promote skin

992        wound healing. *J. Tissue Eng. Regen. Med.* **12**, (2018).

993        38. Takaya, K. *et al.* Fibroblast Growth Factor 7 Suppresses Fibrosis and Promotes  
994        Epithelialization during Wound Healing in Mouse Fetuses. *Int. J. Mol. Sci.* **23**, (2022).

995        39. Ou, Z. *et al.* Single-Nucleus RNA Sequencing and Spatial Transcriptomics Reveal the  
996        Immunological Microenvironment of Cervical Squamous Cell Carcinoma. *Adv. Sci. Lett.*  
997        **9**, 2203040 (2022).

998        40. Tulac, S. *et al.* Identification, characterization, and regulation of the canonical Wnt  
999        signaling pathway in human endometrium. *J. Clin. Endocrinol. Metab.* **88**, 3860–3866  
1000        (2003).

1001        41. Muter, J. *et al.* Progesterone-Dependent Induction of Phospholipase C-Related  
1002        Catalytically Inactive Protein 1 (PRIP-1) in Decidualizing Human Endometrial Stromal  
1003        Cells. *Endocrinology* **157**, 2883 (2016).

1004        42. Tang, M., Naidu, D., Hearing, P., Handwerger, S. & Tabibzadeh, S. LEFTY, a member  
1005        of the transforming growth factor-beta superfamily, inhibits uterine stromal cell  
1006        differentiation: a novel autocrine role. *Endocrinology* **151**, 1320–1330 (2010).

1007        43. Simmons, R. M. *Insulin-like Growth Factor Binding Proteins -1 and -3, and*  
1008        *Hydroxysteroid (11-Beta) Dehydrogenase One: Potential Roles in Ruminant Conceptus*  
1009        *Development and Endometrial Function.* (2010).

1010        44. Brar, A. K., Kessler, C. A., Meyer, A. J., Cedars, M. I. & Jikihara, H. Retinoic acid  
1011        suppresses in-vitro decidualization of human endometrial stromal cells. *Mol. Hum.*  
1012        *Reprod.* **2**, 185–193 (1996).

1013        45. Efremova, M., Vento-Tormo, M., Teichmann, S. A. & Vento-Tormo, R. CellPhoneDB:  
1014        inferring cell-cell communication from combined expression of multi-subunit ligand-  
1015        receptor complexes. *Nat. Protoc.* **15**, 1484–1506 (2020).

1016        46. Vento-Tormo, R. *et al.* Single-cell reconstruction of the early maternal-fetal interface in  
1017        humans. *Nature* **563**, 347–353 (2018).

1018        47. Pace, D., Morrison, L. & Bulmer, J. N. Proliferative activity in endometrial stromal  
1019        granulocytes throughout menstrual cycle and early pregnancy. *J. Clin. Pathol.* **42**, 35–39  
1020        (1989).

1021        48. Flynn, L. *et al.* Menstrual cycle dependent fluctuations in NK and T-lymphocyte subsets  
1022        from non-pregnant human endometrium. *Am. J. Reprod. Immunol.* **43**, 209–217 (2000).

1023        49. Bonatz, G. *et al.* Macrophage- and lymphocyte-subtypes in the endometrium during  
1024        different phases of the ovarian cycle. *Int. J. Gynaecol. Obstet.* **37**, 29–36 (1992).

1025        50. Garry, R., Hart, R., Karthigasu, K. A. & Burke, C. Structural changes in endometrial  
1026        basal glands during menstruation. *BJOG* **117**, 1175–1185 (2010).

1027        51. Werner, S. & Grose, R. Regulation of wound healing by growth factors and cytokines.  
1028        *Physiol. Rev.* **83**, 835–870 (2003).

1029 52. Buechler, M. B., Fu, W. & Turley, S. J. Fibroblast-macrophage reciprocal interactions in  
1030 health, fibrosis, and cancer. *Immunity* **54**, 903–915 (2021).

1031 53. Gelati, M., Aplin, A. C., Fogel, E., Smith, K. D. & Nicosia, R. F. The angiogenic response  
1032 of the aorta to injury and inflammatory cytokines requires macrophages. *J. Immunol.*  
1033 **181**, 5711–5719 (2008).

1034 54. Leibovich, S. J. *et al.* Macrophage-induced angiogenesis is mediated by tumour  
1035 necrosis factor-alpha. *Nature* **329**, 630–632 (1987).

1036 55. Vasse, M. *et al.* Oncostatin M induces angiogenesis in vitro and in vivo. *Arterioscler.*  
1037 *Thromb. Vasc. Biol.* **19**, 1835–1842 (1999).

1038 56. Koch, A. E. *et al.* Interleukin-8 as a macrophage-derived mediator of angiogenesis.  
1039 *Science* **258**, 1798–1801 (1992).

1040 57. Matsumoto, S. *et al.* GREB1 induced by Wnt signaling promotes development of  
1041 hepatoblastoma by suppressing TGF $\beta$  signaling. *Nat. Commun.* **10**, 3882 (2019).

1042 58. Matsumoto, S. *et al.* Wnt Signaling Stimulates Cooperation between GREB1 and  
1043 HNF4a to Promote Proliferation in Hepatocellular Carcinoma. *Cancer Res.* **83**, 2312–  
1044 2327 (2023).

1045 59. Jones, J. I. & Clemmons, D. R. Insulin-like growth factors and their binding proteins:  
1046 biological actions. *Endocr. Rev.* **16**, 3–34 (1995).

1047 60. Aboalola, D. & Han, V. K. M. Different Effects of Insulin-Like Growth Factor-1 and  
1048 Insulin-Like Growth Factor-2 on Myogenic Differentiation of Human Mesenchymal Stem  
1049 Cells. *Stem Cells Int.* **2017**, (2017).

1050 61. Forster, R. *et al.* Macrophage-derived insulin-like growth factor-1 is a key neurotrophic  
1051 and nerve-sensitizing factor in pain associated with endometriosis. *FASEB J.* **33**,  
1052 11210–11222 (2019).

1053 62. García-Gómez, E. *et al.* Regulation of Inflammation Pathways and Inflammasome by  
1054 Sex Steroid Hormones in Endometriosis. *Front. Endocrinol.* **10**, 497959 (2020).

1055 63. Agic, A. *et al.* Is endometriosis associated with systemic subclinical inflammation?  
1056 *Gynecol. Obstet. Invest.* **62**, 139–147 (2006).

1057 64. Giuliani, E., As-Sanie, S. & Marsh, E. E. Epidemiology and management of uterine  
1058 fibroids. *Int. J. Gynaecol. Obstet.* **149**, 3–9 (2020).

1059 65. Mercuri, N. D. & Cox, B. J. Meta-Research: The need for more research into  
1060 reproductive health and disease. (2022) doi:10.7554/eLife.75061.

1061 66. MacLean, J. A. & Hayashi, K. Progesterone Actions and Resistance in Gynecological  
1062 Disorders. *Cells* **11**, 647 (2022).

1063 67. Makieva, S. *et al.* Inside the Endometrial Cell Signaling Subway: Mind the Gap(s). *Int. J.*  
1064 *Mol. Sci.* **19**, (2018).

1065 68. Ni, N. & Li, Q. TGF $\beta$  superfamily signaling and uterine decidualization. *Reprod. Biol.*

1066 15, 1–9 (2017).

1067 69. Xu, S., Chan, R. W. S., Li, T., Ng, E. H. Y. & Yeung, W. S. B. Understanding the  
1068 regulatory mechanisms of endometrial cells on activities of endometrial mesenchymal  
1069 stem-like cells during menstruation. *Stem Cell Res. Ther.* **11**, 1–14 (2020).

1070 70. Bruner, K. L. *et al.* Transforming growth factor beta mediates the progesterone  
1071 suppression of an epithelial metalloproteinase by adjacent stroma in the human  
1072 endometrium. *Proc. Natl. Acad. Sci. U. S. A.* **92**, 7362–7366 (1995).

1073 71. Osteen, K. G., Igarashi, T. M. & Bruner-Tran, K. L. Progesterone action in the human  
1074 endometrium: induction of a unique tissue environment which limits matrix  
1075 metalloproteinase (MMP) expression. *Front. Biosci.* **8**, (2003).

1076 72. Turco, M. Y. *et al.* Long-term, hormone-responsive organoid cultures of human  
1077 endometrium in a chemically defined medium. *Nat. Cell Biol.* **19**, 568–577 (2017).

1078 73. Boretto, M. *et al.* Development of organoids from mouse and human endometrium  
1079 showing endometrial epithelium physiology and long-term expandability. *Development*  
1080 **144**, 1775–1786 (2017).

1081 74. Thiruchelvam, U., Dransfield, I., Saunders, P. T. K. & Critchley, H. O. D. The importance  
1082 of the macrophage within the human endometrium. *J. Leukoc. Biol.* **93**, 217–225 (2013).

1083 75. Salamonsen, L. A. & Woolley, D. E. Menstruation: induction by matrix  
1084 metalloproteinases and inflammatory cells. *J. Reprod. Immunol.* **44**, 1–27 (1999).

1085 76. Thiruchelvam, U. *et al.* Cortisol regulates the paracrine action of macrophages by  
1086 inducing vasoactive gene expression in endometrial cells. *J. Leukoc. Biol.* **99**, 1165–  
1087 1171 (2016).

1088 77. Critchley, H. O., Kelly, R. W., Brenner, R. M. & Baird, D. T. The endocrinology of  
1089 menstruation--a role for the immune system. *Clin. Endocrinol.* **55**, 701–710 (2001).

1090 78. Vallvé-Juanico, J., Houshdaran, S. & Giudice, L. C. The endometrial immune  
1091 environment of women with endometriosis. *Hum. Reprod. Update* **25**, 564–591 (2019).

1092 79. Sbracia, M. *et al.* Differential expression of IGF-I and IGF-II in eutopic and ectopic  
1093 endometria of women with endometriosis and in women without endometriosis. *Am. J.*  
1094 *Reprod. Immunol.* **37**, (1997).

1095 80. Kao, L. C. *et al.* Expression profiling of endometrium from women with endometriosis  
1096 reveals candidate genes for disease-based implantation failure and infertility.  
1097 *Endocrinology* **144**, 2870–2881 (2003).

1098 81. Pazhohan A, Amidi F, Akbari-Asbagh F, Seyedrezazadeh E, Farzadi L, Khodarahmin M,  
1099 Mehdinejadiani S, Sobhani A. The Wnt/β-catenin signaling in endometriosis, the  
1100 expression of total and active forms of β-catenin, total and inactive forms of glycogen  
1101 synthase kinase-3β, WNT7a and DICKKOPF-1. *Eur. J. Obstet. Gynecol. Reprod. Biol.*  
1102 **220**, 1–5 (2018).

1103 82. Gnecco, J. S. *et al.* Organoid co-culture model of the cycling human endometrium in a  
1104 fully-defined synthetic extracellular matrix reveals epithelial-stromal crosstalk. *bioRxiv*  
1105 2021.09.30.462577 (2022) doi:10.1101/2021.09.30.462577.

1106 83. Anderson, C. A. *et al.* Data quality control in genetic case-control association studies.  
1107 *Nat. Protoc.* **5**, 1564–1573 (2010).

1108 84. Chang, C. C. *et al.* Second-generation PLINK: rising to the challenge of larger and  
1109 richer datasets. *Gigascience* **4**, s13742–015–0047–8 (2015).

1110 85. Danecek, P. *et al.* Twelve years of SAMtools and BCFtools. *Gigascience* **10**, (2021).

1111 86. Bayraktar, O. A. *et al.* Astrocyte layers in the mammalian cerebral cortex revealed by a  
1112 single-cell *in situ* transcriptomic map. *Nat. Neurosci.* (2020) doi:10.1038/s41593-020-  
1113 0602-1.

1114 87. Popescu, D.-M. *et al.* Decoding human fetal liver haematopoiesis. *Nature* **574**, 365–371  
1115 (2019).

1116 88. Park, J.-E. *et al.* A cell atlas of human thymic development defines T cell repertoire  
1117 formation. *Science* **367**, (2020).

1118 89. Kleshchevnikov, V. *et al.* Comprehensive mapping of tissue cell architecture via  
1119 integrated single cell and spatial transcriptomics. *Cold Spring Harbor Laboratory*  
1120 2020.11.15.378125 (2020) doi:10.1101/2020.11.15.378125.

1121 90. Garcia-Alonso, L. *et al.* Single-cell roadmap of human gonadal development. *Preprint*  
1122 *from Research Square* (2021) doi:10.21203/rs.3.rs-496470/v1 .

1123 91. Dann, E., Henderson, N. C., Teichmann, S. A., Morgan, M. D. & Marioni, J. C.  
1124 Differential abundance testing on single-cell data using k-nearest neighbor graphs. *Nat.*  
1125 *Biotechnol.* **40**, 245–253 (2022).

1126 92. Elmentait, R. *et al.* Cells of the human intestinal tract mapped across space and time.  
1127 *Nature* **597**, 250–255 (2021).

1128 93. Wakefield, J. A Bayesian measure of the probability of false discovery in genetic  
1129 epidemiology studies. *Am. J. Hum. Genet.* **81**, 208–227 (2007).

1130 94. D'Hooghe, T. *Biomarkers for Endometriosis: State of the Art.* (Springer, 2017).

1131 **Acknowledgements**

1132 This publication is part of the Human Cell Atlas – [www.humancellatlas.org/publications/](http://www.humancellatlas.org/publications/). The  
1133 authors would like to thank the participants of the ENDOX and FENOX studies in the Oxford  
1134 Endometriosis CaRe Centre for donating samples and data. We are also grateful to the  
1135 transplant organ donors and their families for the samples donated through the Cambridge  
1136 Biorepository for Translational Medicine. We would also like to thank Kelly Barrett, Carol  
1137 Hubbard and Lisa Buck for patient recruitment and clinical sample collection; the Sanger  
1138 Cellular Generation and Phenotyping (CGaP) Core Facility, Sanger Core Sequencing pipeline  
1139 for support with sample processing and sequencing library preparation; Martin Prete and

1140 Simon Murray for insightful comments and web portal support; Tarryn Porter and the Cellular  
1141 Genetics wet lab team for experimental support; Antonio García from Bio-Graphics for  
1142 scientific illustrations; Aidan Maartens for proofreading.

1143

1144 **Funding:** This research was funded in part, by the Wellcome Trust Grant 206194 and  
1145 220540/Z/20/A and 203141/Z/16/Z; the European Union's Horizon 2020 research and  
1146 innovation programme HUTER under grant agreement No 874867; grant number 2022-  
1147 249429(5022) from the Chan Zuckerberg Foundation; and the John Fell Fund from the  
1148 University of Oxford. M.Ma is funded by the Medical Research Council. Sample collection at  
1149 Imperial was supported by Borne, grant no P84654.

## 1150 **Author information**

1151 R.V.T, M.Ma, and L.G-A conceived and designed the experiments and analyses. L.G-A  
1152 analysed the data with contributions from M.Ma, M.Mo, V.L, S.H, M.K and M.L. M.Ma, C.S.S.  
1153 and A.O. performed sample processing. C.I.M performed the imaging experiments. L.G-A and  
1154 R.P developed the cell-cell communication platform. K.Ga oversaw patient metadata  
1155 collection for ENDOX and FENOX studies. Ke.G and S.Y performed menstrual cycle staging.  
1156 E.V.W, V.M, K.T.M, K.S-P and I.G. collected some of the samples analysed. M.Ma, L.G-A and  
1157 R.V.T. interpreted the data with contributions from M.Mo, V.L, and S.H. M.Ma, L.G-A and  
1158 R.V.T wrote the manuscript. R.V-T and K.T.Z supervised the work with contributions from  
1159 C.M.B, R.A.D and J.S. All authors read and approved the manuscript.

## 1160 **Competing interests**

1161 K.T.Z and C.M.B have received grant funding from Bayer AG, AbbVie Inc., Roche Diagnostics  
1162 Inc., Volition Rx, MDNA Life Sciences, and Precision Life, unrelated to the work presented in  
1163 this paper. K.T.Z is also a Board member of the World Endometriosis Research Foundation.  
1164 The remaining authors declare no competing interests.

1165 **Figure legends**

1166 **Figure 1. Harmonised cellular map of the human endometrium.** **a**, Schematic illustration  
1167 of the human uterus and cellular composition of the endometrium as it undergoes  
1168 morphological changes across the menstrual cycle. **b**, List of datasets analysed and  
1169 contribution of the number of donors, cells/nuclei, endometrial histology and endometriosis  
1170 status of all samples profiled per dataset. **c**, UMAP projections of scRNA-seq data from a total  
1171 of 63 individuals and ~314,000 cells coloured by cell state. **d**, UMAP projections of snRNA-  
1172 seq data from a total of 63 individuals and ~312,000 nuclei coloured by cell state. **e**, Bar plot  
1173 showing the contribution of each of the scRNA-seq datasets to the main cellular lineages  
1174 (endothelial, epithelial, immune and mesenchymal lineages) as shown in c. **f**, Bar plot showing  
1175 the cellular composition of endometrial biopsies from the proliferative ( $n = 25$ ), early secretory  
1176 ( $n = 6$ ), early/mid secretory ( $n = 7$ ), mid secretory ( $n = 6$ ) and late secretory ( $n = 1$ ) phases of  
1177 the menstrual cycle for the scRNA-seq data presented in c. dStromal, decidualised stromal  
1178 cells; eStromal, endometrial stromal cells specific to proliferative phase; HECA, human  
1179 endometrial cell atlas; MMPs, matrix metalloproteinases; mPV, myometrial perivascular cells;  
1180 ePV, endometrial perivascular cells; scRNA-seq, single-cell RNA-sequencing; secret.,  
1181 secretory; snRNA-seq, single-nucleus RNA-sequencing; UMAP, uniform manifold  
1182 approximation and projection; uSMCs, uterine smooth muscle cells.  
1183

1184 **Figure 2. Spatiotemporal complexity of epithelial cells.** **a**, Dot plot showing normalised,  
1185 log-transformed and variance-scaled expression of genes (x-axis) characteristic of the  
1186 identified epithelial cell states (y-axis) in scRNA-seq data. **b**, Visium spatial transcriptomics  
1187 data and an H&E image of the same tissue section are shown. Spot colour indicates estimated  
1188 cell state density for the SOX9 basalis (CDH2+) population in each Visium spot, as computed  
1189 by cell2location. Spatial mapping of the SOX9 basalis (CDH2+) population is shown in  
1190 sections of whole-uterus biopsies from donors A13 (proliferative phase) and A30 (secretory  
1191 phase). **c**, High-resolution multiplexed smFISH of a section of a whole-uterus biopsy from  
1192 donor A13 stained for *DAPI* (white, nuclei), *EPCAM* (magenta, epithelial cells), *SOX9* (yellow,  
1193 epithelial cells), *CDH2* (red, epithelial cells). The dotted line highlights the *basalis* area of the  
1194 endometrium where signal for all markers and their co-localisation is detected within the  
1195 epithelial glands. The inset shows a representative zoom-in of one of the glands and signal  
1196 co-localisation. Scale bars = 100  $\mu$ m. **d**, Dot plot showing normalised, log-transformed and  
1197 variance-scaled expression of *CXCR4* and *CXCL12* (x-axis) in a selection of epithelial and  
1198 mesenchymal cells (y-axis) in scRNA-seq data. Asterisk denotes a significant cell-cell  
1199 interaction identified through CellPhoneDB analyses. **e**, Left, high-resolution multiplexed  
1200 smFISH of a section of a superficial biopsy from donor FX1233 showing the expression of  
1201 *DAPI* (white, nuclei), *EPCAM* (magenta, epithelial cells), *CBR3* (cyan, preGlandular cells), and  
1202 *OPRK1* (yellow, preGlandular cells). The dashed outlines indicate areas shown magnified to  
1203 the right. Top right, a magnified image of the luminal region with low *OPRK1* and *CBR3* signal.  
1204 Bottom right, a magnified image of the glandular region with high and co-localised *OPRK1* and  
1205 *CBR3* signal. Scale bars = 100  $\mu$ m. **f**, Visium spatial transcriptomics data and an H&E image  
1206 of the same tissue section are shown. Spot colour indicates estimated cell state density for  
1207 the preLuminal, Luminal, preGlandular and Glandular populations in each Visium spot, as  
1208 computed by cell2location. Spatial mapping of preLuminal, Luminal, preGlandular and  
1209 Glandular populations is visualised in a section of a superficial biopsy from donor FX0028  
1210 (early secretory phase) and a section of a whole-uterus biopsy from donor A30 (mid secretory  
1211 phase). **g**, Schematic illustration of the spatiotemporal complexity of the endometrial

1212 epithelium across the proliferative and secretory phases. eStromal, endometrial stromal cells  
1213 specific to proliferative phase; MMPs, matrix metalloproteinases; Prolif., proliferative; smFISH,  
1214 single molecule fluorescence in situ hybridisation; uSMCs, uterine smooth muscle cells.

1215  
1216 **Figure 3. Endometrial stromal cell heterogeneity and stromal-epithelial cell cross-talk**  
1217 **across the menstrual cycle.** **a**, Dot plot showing normalised, log-transformed and variance-  
1218 scaled expression of genes (x-axis) characteristic of the identified stromal cell states (y-axis)  
1219 in scRNA-seq data. **b**, Visium spatial transcriptomics data and an H&E image of the same  
1220 tissue section are shown. Spot colour indicates estimated cell state density for a specific cell  
1221 population in each Visium spot as computed by cell2location. Spatial mapping of the eStromal,  
1222 dStromal early and dStromal mid cell populations is shown in a section of a whole-uterus  
1223 biopsy from donor A13 (top panel, proliferative phase), a section of a superficial biopsy from  
1224 donor FX0033 (middle panel, early secretory phase) and a section of a whole-uterus biopsy  
1225 from donor A30 (bottom panel, mid secretory phase). Mapping of menstrual cycle phase-  
1226 relevant epithelial cell populations is also shown in the niche composition panel. **c**, Dot plot  
1227 showing normalised, log-transformed and variance-scaled expression of genes (x-axis) in  
1228 epithelial and mesenchymal cell states (y-axis) in scRNA-seq data. Signalling ligands involved  
1229 in TGF $\beta$ , insulin, retinoic acid and WNT signalling are shown. **d**, Schematic illustration of the  
1230 temporal complexity of endometrial stromal cells and signalling pathways across the  
1231 proliferative and secretory phases. eStromal, endometrial stromal cells specific to proliferative  
1232 phase; dStromal, decidualised stromal cells; MMPs, matrix metalloproteinases; RA, retinoic  
1233 acid; TGF $\beta$ , transforming growth factor beta.

1234  
1235 **Figure 4. Predicted ligand-receptor interactions and role of macrophages in**  
1236 **endometrial repair and regeneration.** **a**, Left, UMAP projections of scRNA-seq data for  
1237 32,322 immune cells coloured by cell type. Right, UMAP projections of snRNA-seq data for  
1238 24,820 immune cells/nuclei coloured by cell type. **b**, Beeswarm plot of the distribution of log  
1239 fold change across the menstrual cycle (proliferative and secretory phases) in neighbourhoods  
1240 containing immune cells from different cell type clusters in scRNA-seq data. Differentially  
1241 abundant neighbourhoods at log fold change  $> 2.5$  and spatial FDR  $< 0.1$  are coloured. **c**, Dot  
1242 plot showing normalised, log-transformed and variance-scaled expression of genes (y-axis) in  
1243 uNK and uM cell states (x-axis) in scRNA-seq data. Asterisk denotes significantly upregulated  
1244 expression at FDR  $< 0.05$ . **d**, Dot plots showing normalised, log-transformed and variance-  
1245 scaled expression of signalling molecules and receptors (y-axes) upregulated in uNK, uM and  
1246 stromal cell states (x-axes) in scRNA-seq data. Asterisk denotes significantly upregulated  
1247 expression at FDR  $< 0.05$ . The predicted cell-cell communication between uNK, uM and  
1248 stromal cell states, including its likely role, is shown by differently coloured arrows. **e**, Dot plot  
1249 showing normalised, log-transformed and variance-scaled expression of pro-angiogenic  
1250 signalling molecules (y-axis) upregulated in uNK and uM cell states (x-axis) in scRNA-seq  
1251 data. Asterisk denotes significantly upregulated expression at FDR  $< 0.05$ . **f**, Schematic  
1252 illustration of macrophage and stromal cell signalling during the menstrual and proliferative  
1253 phases, likely involved in macrophage cell recruitment, increasing wound healing abilities and  
1254 dampening inflammation in stromal cells. **g**, Schematic illustration of macrophage, endothelial  
1255 cell and perivascular cell signalling likely involved in macrophage recruitment and  
1256 angiogenesis. Cells from donors on hormones and donors with endometriosis were excluded  
1257 from analyses shown in **b** - **e** of this figure. cDC, conventional dendritic cells; dStromal,  
1258 decidualised stromal cells; eStromal, endometrial stromal cells specific to proliferative phase;  
1259 FDR, false discovery rate; ILC3, innate lymphoid cell type 3; MMPs, matrix metalloproteinases;

1260 pDC, plasmacytoid dendritic cell; scRNA-seq, single-cell RNA-sequencing; snRNA-seq,  
1261 single-nucleus RNA-sequencing; T Reg, T regulatory cells; UMAP, uniform manifold  
1262 approximation and projection; uM, uterine macrophages; uNK, uterine natural killer cells.  
1263

1264 **Figure 5. Endometrial stromal-immune cell niche in endometriosis.** **a**, Beeswarm plot of  
1265 the distribution of log fold change between conditions (controls and endometriosis cases) in  
1266 neighbourhoods containing endometrial cells from different cell type clusters in snRNA-seq  
1267 data. Differentially abundant neighbourhoods at log fold change  $> 2.5$  and spatial FDR  $< 0.1$   
1268 are coloured. **b**, Forest plot showing the log odds ratio (x-axis) of the enrichment for expression  
1269 of genes associated with endometriosis in each endometrial cell type (y-axis). Cell types in  
1270 orange have FDR  $< 0.05$ . **c**, Dot plot showing normalised, log-transformed and variance-  
1271 scaled expression of differentially expressed genes (x-axis) in dStromal cell states of controls  
1272 and endometriosis cases (y-axis) in scRNA-seq data. **d**, Dot plot showing normalised, log-  
1273 transformed and variance-scaled expression of differentially expressed genes (x-axis)  
1274 upregulated in uM cell states (y-axis) in scRNA-seq data. Cells from donors on hormones were  
1275 excluded from all analyses shown in this figure. dStromal, decidualised stromal cells; FDR,  
1276 false discovery rate; uM, uterine macrophages.

## 1277 **Supplementary Material**

### 1278 **Supplementary Figures**

1279 **Supplementary Figure 1. Single-cell RNA-sequencing datasets of the Human**  
1280 **Endometrial Cell Atlas (HECA) and the cervix.** **a**, UMAP projections of scRNA-seq data for  
1281 HECA coloured by cell lineage, dataset, menstrual cycle group, cell cycle phase and biopsy  
1282 type. **b**, Dot plot showing normalised, log-transformed and variance-scaled expression of  
1283 genes (x-axis) characteristic of the main cell lineage (y-axis) in the HECA. **c**, Dot plot showing  
1284 normalised, log-transformed and variance-scaled expression of genes (x-axis) characteristic  
1285 of a selection of mesenchymal and endothelial cells (y-axis) in the HECA. **d**, Bar plot showing  
1286 the cellular composition of endometrial biopsies belonging to the different menstrual cycle  
1287 groups (y-axis). **e**, UMAP projection of a scANVI representation of the HECA coloured by the  
1288 cell states identified. The MUC5B, KRT5 and HOXA13 populations are outlined by red dotted-  
1289 lined shapes. **f**, UMAP projection of the Liu et al. 2023 scRNA-seq dataset of the human cervix  
1290 coloured by louvain clusters and their correspondence to the four main cell lineages (epithelial,  
1291 endothelial, mesenchymal and immune). **g**, Dot plot showing normalised, log-transformed and  
1292 variance-scaled expression of genes (x-axis) characteristic of the cell clusters identified in the  
1293 Liu et al. 2023 cervix dataset (y-axis). Highlighted by purple rectangles are the epithelial and  
1294 mesenchymal clusters that expressed markers characteristic of the MUC5B, KRT5 and  
1295 HOXA13 cell populations defined in the HECA. **h**, UMAP projection of the mapping of the Liu  
1296 et al. 2023 cervix dataset onto the scANVI representation of the HECA coloured by the cell  
1297 states identified in the HECA and the Liu et al. 2023 cervix dataset (dark grey). The MUC5B,  
1298 KRT5 and HOXA13 populations of the HECA are outlined by red dotted-lined shapes. **i**, UMAP  
1299 projection of the mapping of the Liu et al. 2023 cervix dataset onto the scANVI representation  
1300 of the HECA coloured by the cell clusters identified in the Liu et al. 2023 cervix dataset. The  
1301 MUC5B, KRT5 and HOXA13 populations of the HECA are outlined by red dotted-lined shapes.  
1302 dStromal, decidualised stromal cells; ePV, endometrial perivascular cells; eStromal,  
1303 endometrial stromal cells specific to proliferative phase; HECA, human endometrial cell atlas;  
1304 MMPs, matrix metalloproteinases; NK, natural killer cells; scRNA-seq, single-cell RNA-  
1305 sequencing; scANVI, single-cell ANnotation using Variational Inference; T, T cells; UMAP,  
1306 uniform manifold approximation and projection; uSMCs, uterine smooth muscle cells.

1307

1308 **Supplementary Figure 2. Single-nucleus RNA-sequencing cell state identification and**  
1309 **marker gene expression.** **a**, UMAP projections of the snRNA-seq data coloured by cell  
1310 lineage, cell cycle phase, menstrual cycle group, and endometriosis status. **b**, UMAP  
1311 projections of the epithelial cell lineage of the snRNA-seq dataset coloured by the identified  
1312 epithelial cell states of the HECA as assigned by label transfer. **c**, UMAP projections of the  
1313 mesenchymal cell lineage of the snRNA-seq dataset coloured by the identified mesenchymal  
1314 cell states of the HECA as assigned by label transfer. **d**, Dot plot showing normalised, log-  
1315 transformed and variance-scaled expression of genes (x-axis) characteristic of the endothelial  
1316 and immune nuclei (y-axis). **e**, Bar plot showing the cellular composition of endometrial  
1317 biopsies belonging to the different menstrual cycle groups (y-axis). **f**, Dot plot showing  
1318 normalised, log-transformed and variance-scaled expression of genes (x-axis) characteristic  
1319 of the identified epithelial cell states (y-axis) in snRNA-seq data. **g**, Dot plot showing  
1320 normalised, log-transformed and variance-scaled expression of genes (x-axis) characteristic  
1321 of the identified mesenchymal cell states (y-axis) in snRNA-seq data. dStromal, decidualised

1322 stromal cells; ePV, endometrial perivascular cells; eStromal, endometrial stromal cells specific  
1323 to proliferative phase; HECA, human endometrial cell atlas; MMPs, matrix metalloproteinases;  
1324 mPV, myometrial perivascular cells; Prolif., proliferative; secret., secretory; snRNA-seq,  
1325 single-nucleus RNA-sequencing; UMAP, uniform manifold approximation and projection;  
1326 uSMCs, uterine smooth muscle cells.

1327

1328 **Supplementary Figure 3. Cellular heterogeneity of samples from donors taking**  
1329 **exogenous hormones in scRNA-seq and snRNA-seq data.** **a**, UMAP projections of the  
1330 scRNA-seq data coloured by hormonal treatment taken. **b**, Overview of the number of donors  
1331 and cells per hormonal treatment taken in each dataset profiled by scRNA-seq. **c**, Bar plot  
1332 showing the cellular composition of endometrial biopsies from donors taking the different  
1333 hormonal treatment (y-axis) in the scRNA-seq data. **d**, UMAP projections of the snRNA-seq  
1334 data coloured by hormonal treatment taken. **e**, Overview of the number of donors and cells  
1335 per hormonal treatment taken profiled by snRNA-seq. **c**, Bar plot showing the cellular  
1336 composition of endometrial biopsies from donors taking the different hormonal treatment (y-  
1337 axis) in the snRNA-seq dataset. dStromal, decidualised stromal cells; ePV, endometrial  
1338 perivascular cells; eStromal, endometrial stromal cells specific to proliferative phase; MMPs,  
1339 matrix metalloproteinases; mPV, myometrial perivascular cells; Prolif., proliferative; scRNA-  
1340 seq; single-cell RNA-sequencing; secret., secretory; snRNA-seq, single-nucleus RNA-  
1341 sequencing; UMAP, uniform manifold approximation and projection; uSMCs, uterine smooth  
1342 muscle cells.

1343

1344 **Supplementary Figure 4. Spatial transcriptomics mapping of epithelial cell populations.**  
1345 **a**, Visium spatial transcriptomics data and an H&E image of the same tissue section are  
1346 shown. Spot colour indicates estimated cell state density for a specific population in each  
1347 Visium spot, as computed by cell2location. Spatial mapping of the SOX9 functionalis I  
1348 (CDH2+) and SOX9 functionalis II populations is shown in a section of a whole-uterus biopsy  
1349 from donor A13. **b**, Visium spatial transcriptomics data and an H&E image of the same tissue  
1350 section are shown. Spot colour indicates estimated cell state density for a specific population  
1351 in each Visium spot, as computed by cell2location. Spatial mapping of the preLuminal,  
1352 Luminal, preGlandular and Glandular populations is visualised in a section of a superficial  
1353 biopsy from donor FX0033 (early secretory phase). **c**, High-resolution multiplexed smFISH of  
1354 a section of a superficial biopsy from donor FX9006 (early secretory phase) showing the  
1355 expression of *DAPI* (white, nuclei), *EPCAM* (magenta, epithelial cells), *CBR3* (cyan,  
1356 preGlandular cells), and *OPRK1* (yellow, preGlandular cells). The dashed outline indicates the  
1357 area shown magnified to the right. The magnified image shows the glandular region with high  
1358 and co-localised *OPRK1* and *CBR3* signal. White arrows indicate luminal regions with low  
1359 *OPRK1* and *CBR3* signal. **d**, High-resolution multiplexed smFISH of full thickness  
1360 endometrium sections from the proliferative phase (donors A66 and A13) and secretory phase  
1361 (donor A30) showing the expression of *DAPI* (white, nuclei), *EPCAM* (magenta, epithelial  
1362 cells), and *MUC5B* (yellow, epithelial cells). For each panel, the dashed outline indicates the  
1363 area shown magnified. Asterisks indicate some of the regions where the *MUC5B* signal was  
1364 detected and varied across samples. Scale bars are 100  $\mu$ m, unless differently specified.  
1365 smFISH, single molecule fluorescence in situ hybridisation.

1366

1367 **Supplementary Figure 5. Expression of receptors involved in TGF $\beta$ , insulin, retinoic  
1368 acid and WNT signalling.** Dot plot showing normalised, log-transformed and variance-scaled  
1369 expression of genes coding for TGF $\beta$ , insulin, retinoic acid and WNT signalling receptors (x-

1370 axis) in the epithelial and mesenchymal cell states identified (y-axis) in the scRNA-seq data.  
1371 eStromal, endometrial stromal cells specific to proliferative phase; dStromal, decidualised  
1372 stromal cells; MMPs, matrix metalloproteinases; scRNA-seq, single-cell RNA-sequencing;  
1373 TGF $\beta$ , transforming growth factor beta; uSMCs, uterine smooth muscle cells.  
1374

1375 **Supplementary Figure 6. Immune cells in scRNA-seq and snRNA-seq data.** **a**, UMAP  
1376 projections of scRNA-seq data for immune cells coloured by dataset, menstrual cycle group,  
1377 cell cycle phase and biopsy type. **b**, UMAP projections of snRNA-seq data for immune cells  
1378 coloured by menstrual cycle group and cell cycle phase. **c**, UMAP projection of snRNA-seq  
1379 data for immune cells coloured by the probability of assigning the immune cell types identified  
1380 in the scRNA-seq data. Support Vector Machine (SVM) classifier was trained using the  
1381 immune cell scRNA-seq data and the predicted cell type annotations were then projected onto  
1382 the snRNA-seq data with the probability shown. **d**, Dot plot showing normalised, log-  
1383 transformed and variance-scaled expression of genes (x-axis) characteristic of the identified  
1384 immune cell states (y-axis) in the scRNA-seq data. **e**, Dot plot showing normalised, log-  
1385 transformed and variance-scaled expression of genes (x-axis) characteristic of the identified  
1386 immune cell states (y-axis) in the snRNA-seq data. **f**, Beeswarm plot of the distribution of log  
1387 fold change across the menstrual cycle (proliferative and secretory phases) in neighbourhoods  
1388 containing immune cells from different cell type clusters in snRNA-seq data. Differentially  
1389 abundant neighbourhoods at log fold change  $> 2.5$  and spatial FDR  $< 0.1$  are coloured. **g**,  
1390 Visium spatial transcriptomics data for donors A13 (proliferative phase) and A30 (secretory  
1391 phase) are shown. Spot colour indicates estimated cell state density for a specific population  
1392 of perivascular cells (mPV, ePV-1a, ePV-1b and ePV-2) in each Visium spot, as computed by  
1393 cell2location. **h**, Dot plot showing normalised, log-transformed and variance-scaled  
1394 expression of genes (x-axis) characteristic of the identified endothelial, perivascular and  
1395 stromal cells (y-axis) in the scRNA-seq data. cDC, conventional dendritic cells; eStromal,  
1396 endometrial stromal cells specific to proliferative phase; ePV, endometrial perivascular cells;  
1397 FDR, false discovery rate; ILC3, innate lymphoid cell type 3; mPV, myometrial perivascular  
1398 cells; pDC, plasmacytoid dendritic cells; RBC, red blood cells; scRNA-seq, single-cell RNA-  
1399 sequencing; snRNA-seq, single-nucleus RNA-sequencing; SVM, support vector machine; T  
1400 Reg, T regulatory cells; uM, uterine macrophages; UMAP, uniform manifold approximation  
1401 and projection; uNK, uterine natural killer cells.  
1402

1403 **Supplementary Figure 7. Predicted cell-cell interactions underpinning endometrial**  
1404 **regeneration and angiogenesis.** **a**, Dotplot plot reporting the variance-scaled mean  
1405 expression of the two or more (if heteromeric complexes) transcripts coding for the interacting  
1406 proteins in pairs of cell types. Red circles indicate that at least one of the interacting partners  
1407 is differentially expressed in one of the cell types in the pair. Interactions are classified based  
1408 on whether they are predicted to play a role in recruitment, wound healing or  
1409 immunomodulation during endometrial regeneration. **b**, Dotplot plot reporting the variance-  
1410 scaled mean expression of the two or more (if heteromeric complexes) transcripts coding for  
1411 the interacting proteins in pairs of cell types. Red circles indicate that at least one of the  
1412 interacting partners is differentially expressed in one of the cell types in the pair. Interactions  
1413 are classified based on whether they are predicted to play a role in cell recruitment or pro-  
1414 angiogenic processes within the vascular niche.

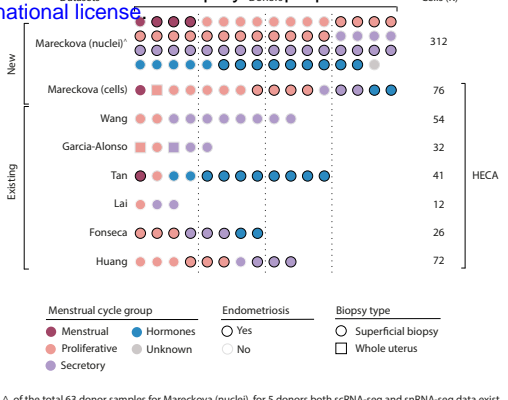
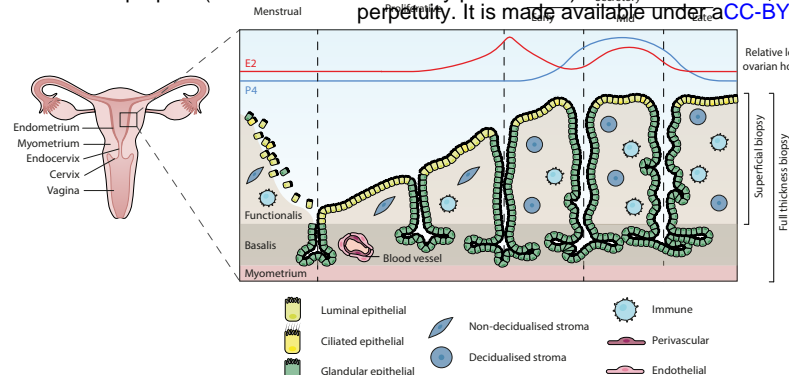
1415   Supplementary Tables

1416   **Supplementary Table 1:** Harmonised metadata of samples analysed.  
1417   **Supplementary Table 2:** CellRanger QC outputs for all newly generated data.  
1418   **Supplementary Table 3:** Differentially expressed genes reported for stromal cells.  
1419   **Supplementary Table 4:** Differentially expressed genes reported for macrophages.  
1420   **Supplementary Table 5:** Reagents used for the snRNA-seq homogenisation buffer.  
1421   **Supplementary Table 6:** Reagents used for the snRNA-seq wash buffer.  
1422   **Supplementary Table 7:** List of smFISH probes used for smFISH imagining.

**Figure 1**

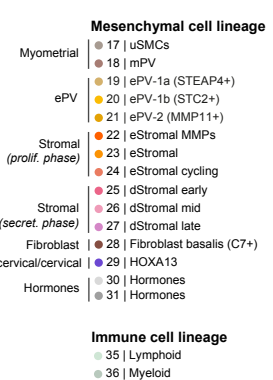
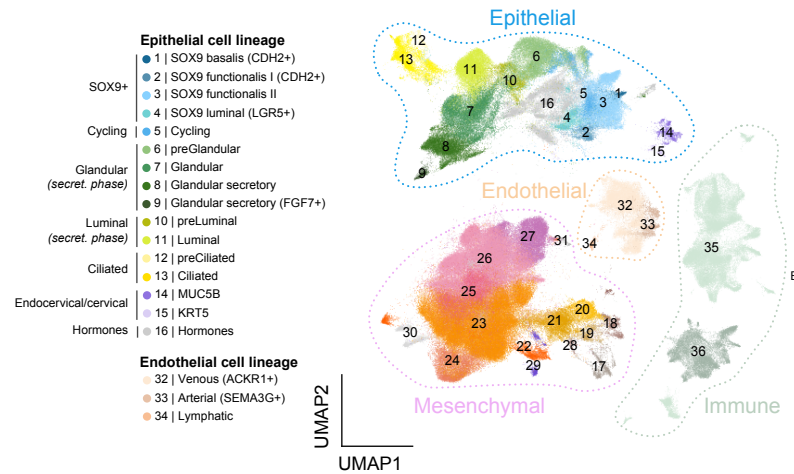
bioRxiv preprint doi: <https://doi.org/10.1101/2023.11.03.564728>; this version posted November 5, 2023. The copyright holder for this preprint (which was not certified by peer review) is the author/funder, who has granted bioRxiv a license to display the preprint in perpetuity. It is made available under aCC-BY-NC-ND 4.0 International license.

### Cells (K)

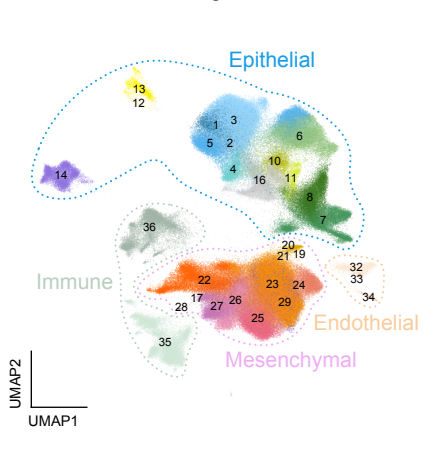


## HECA: Single-cell data

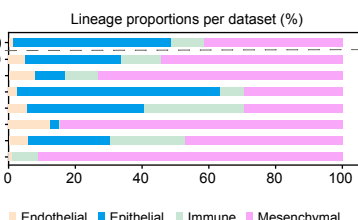
Unified map of all 7 single-cells datasets



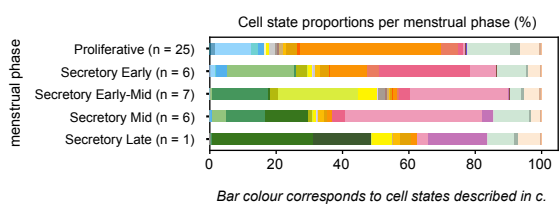
## Single-nuclei data



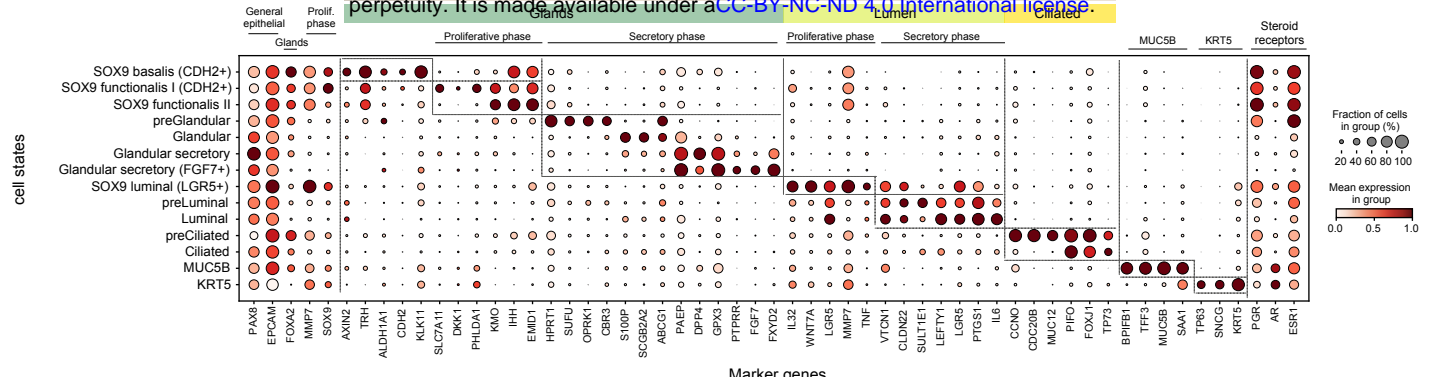
e



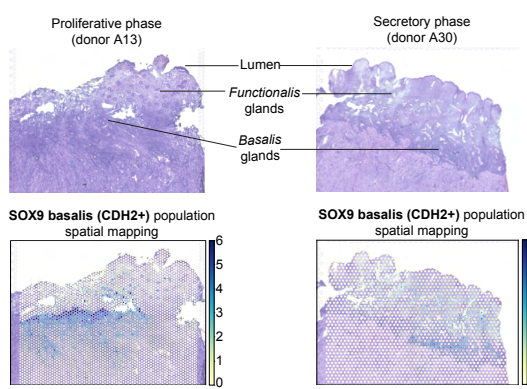
menstrual phase



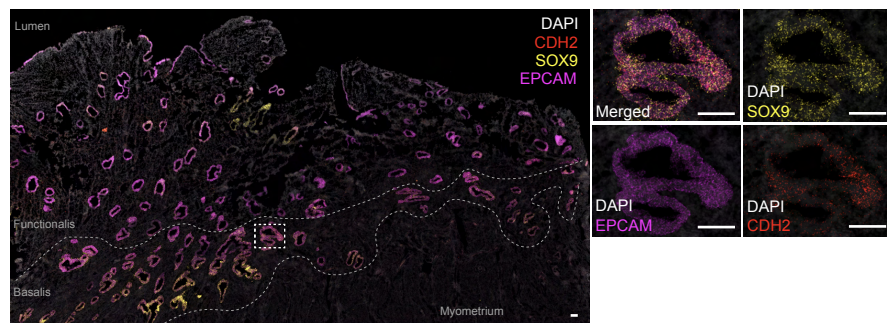
a



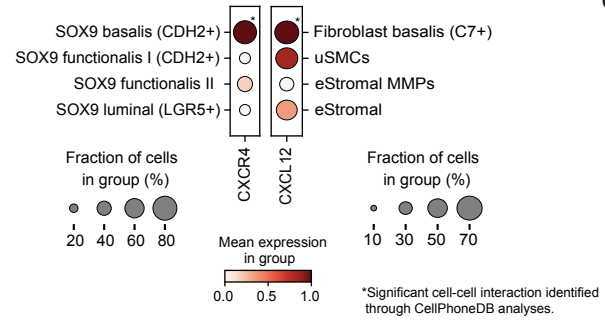
b



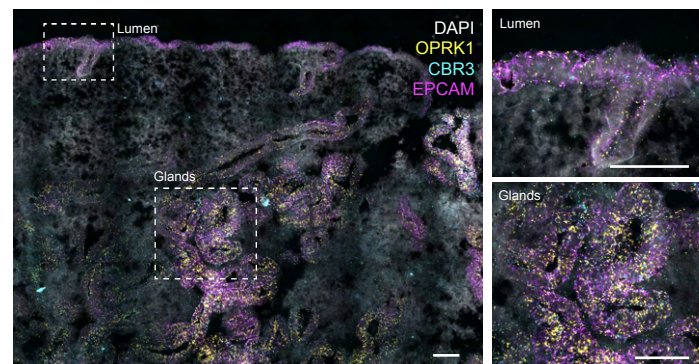
c



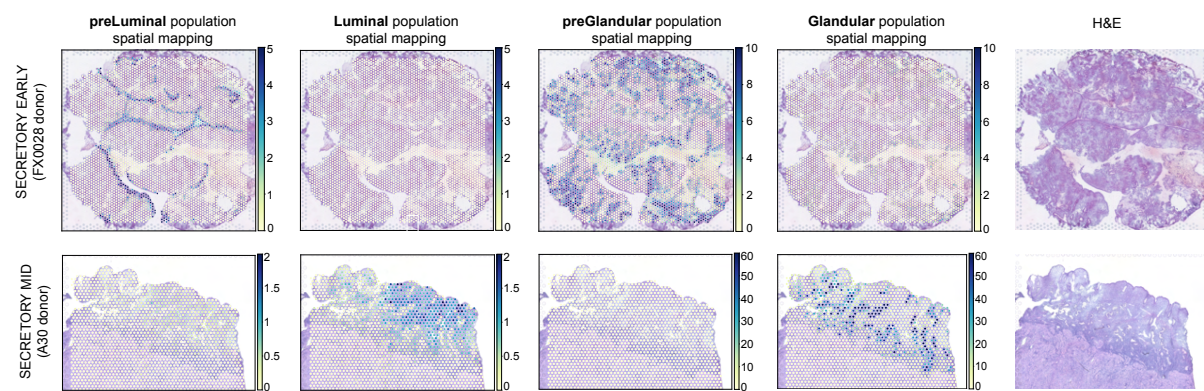
d



e



f



g

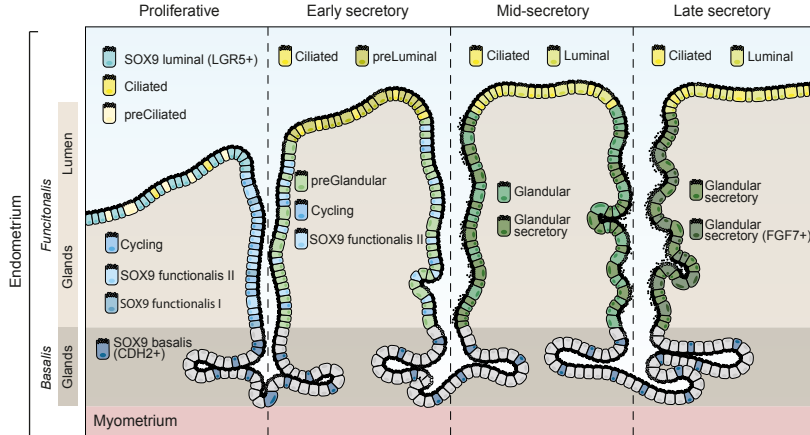
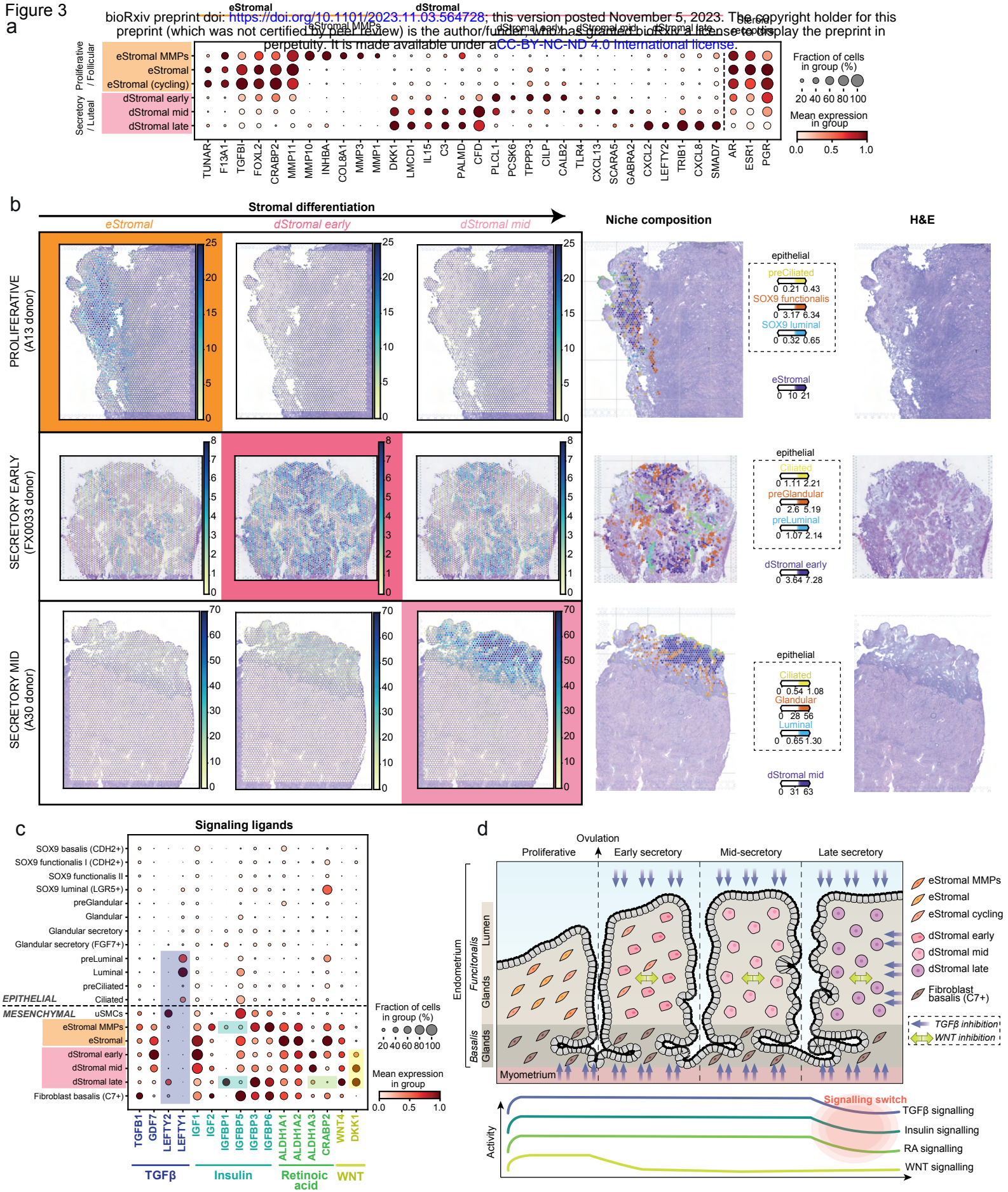
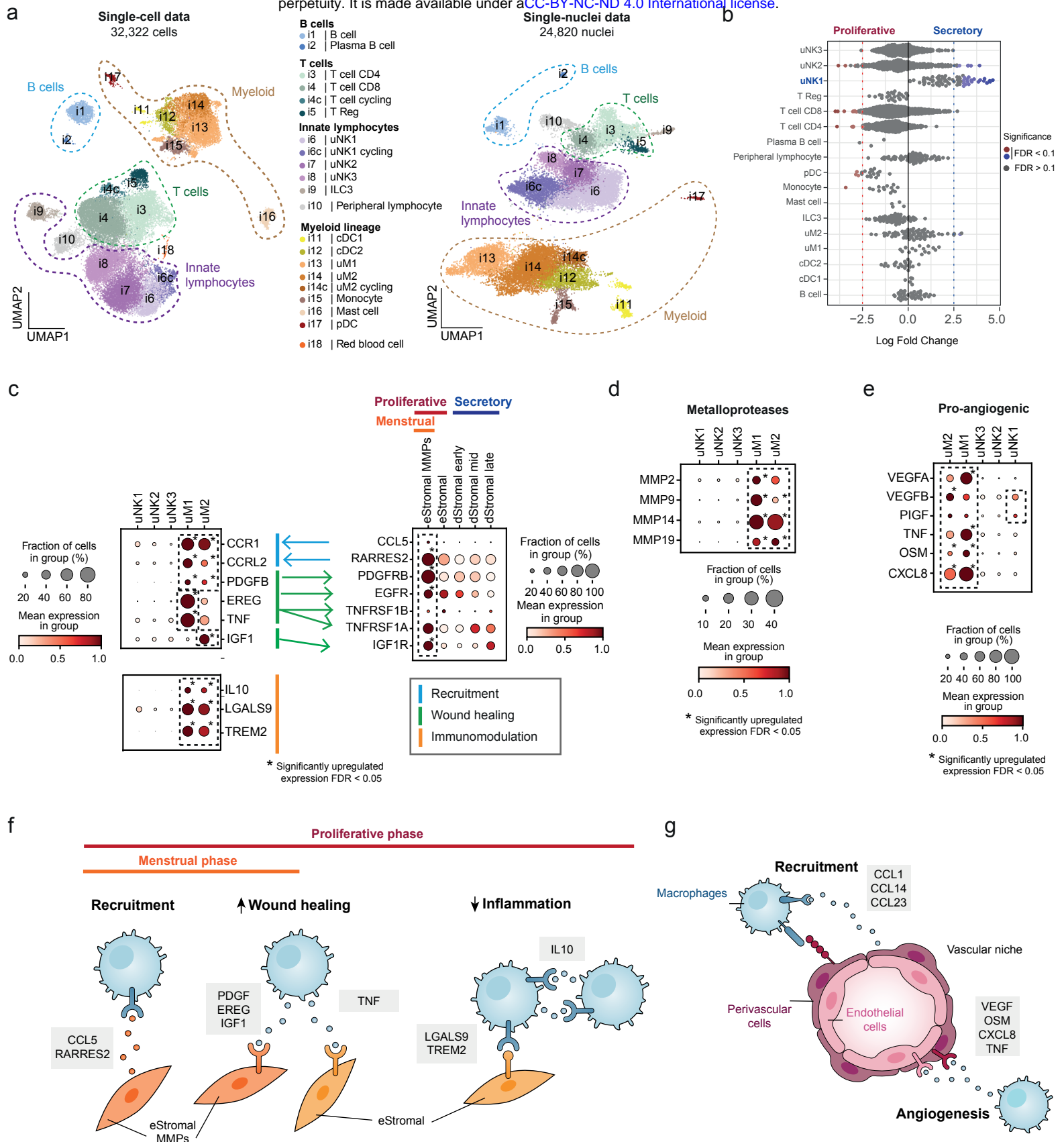


Figure 3

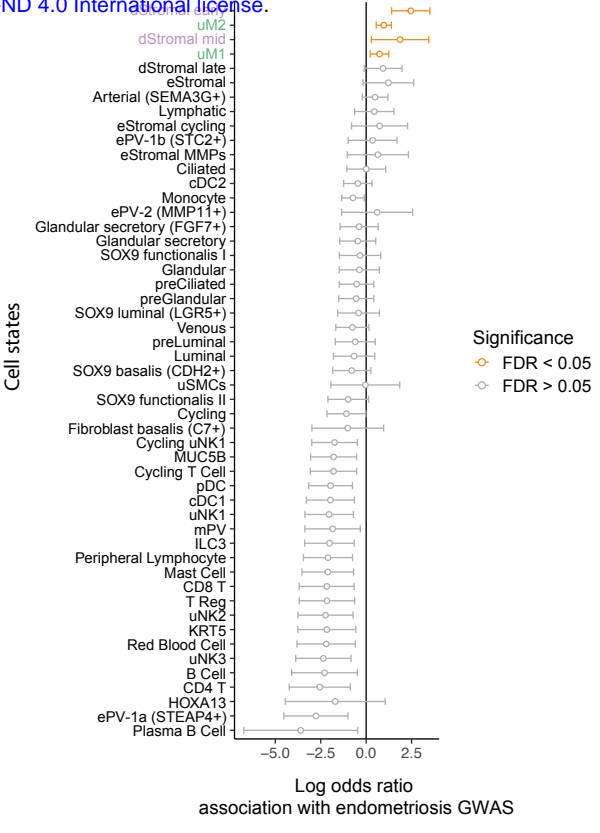
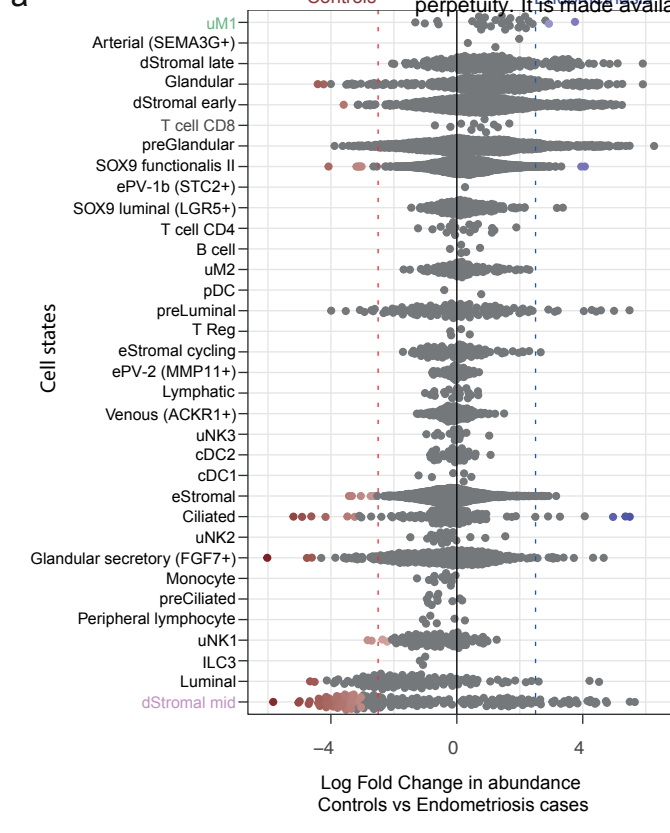


**Figure 4** bioRxiv preprint doi: <https://doi.org/10.1101/2023.11.03.564728>; this version posted November 5, 2023. The copyright holder for this preprint (which was not certified by peer review) is the author/funder, who has granted bioRxiv a license to display the preprint in perpetuity. It is made available under aCC-BY-NC-ND 4.0 International license.

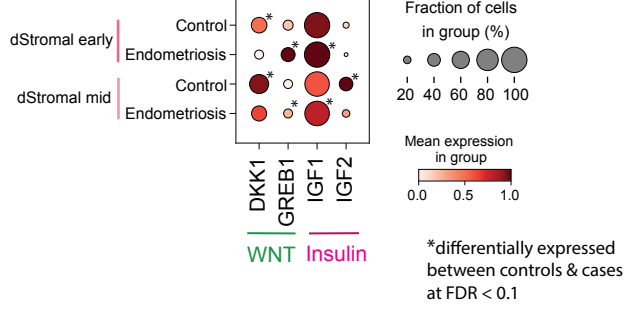


**Figure 5** bioRxiv preprint doi: <https://doi.org/10.1101/2023.11.03.564728>; this version posted November 5, 2023. The copyright holder for this preprint (which was not certified by peer review) is the author/funder, who has granted bioRxiv a license to display the preprint in perpetuity. It is made available under aCC-BY-NC-ND 4.0 International license.

a



c



d

